

# Studies of Molecular and Cluster Fragmentation Using Synchrotron Radiation: Measurements and Models

Lindgren, Andreas

2006

# Studies of Molecular and Cluster Fragmentation Using Synchrotron Radiation: Measurements and Models

Andreas Lindgren

Department of Synchrotron Radiation Research
Lund University

THESIS FOR DEGREE OF DOCTOR OF PHILOSOPHY IN PHYSICS

Faculty Opponent:
Lecturer John H. D. Eland
Oxford University
United Kingdom


LUND
UNIVERSITY

To be presented with the permission of the Faculty of Science of Lund University for public critique in Lecture Hall B at the Department of Physics, October 6 2006, at 10:15.

STUDIES OF MOLECULAR AND CLUSTER FRAGMENTATION USING SYNCHROTRON RADIATION: MEASUREMENTS AND MODELS


Printed in Lund, Sweden, 2006, by Mediatryck.

Department of Synchrotron Radiation Research
Institute of Physics
Lund University
BOX 118
221 00 LUND, SWEDEN

ISBN 13: 978-91-628-6892-5
ISBN 10: 91-628-6892-6

ISRN LUNDFD6/NFSF – 06/1029 – SE

Till Linda

# Abstract

A new spectrometer for studying photoinduced fragmentation has been designed and commissioned. The instrument produces a detailed view of the energy and angular emission of fragments, which in the case of small molecules can be related to their geometry at the moment of dissociation. The spectral profiles for single, double and triple ion coincidences are analyzed in terms of molecular alignment, and nuclear dynamics. A model based upon molecular symmetry and dipole excitation was developed for interpreting multi-coincidence spectra where all ionic fragments are measured. The basic principles of the model can be applied to higher-order fragmentation processes as well, and a picture of molecular dynamics has been obtained.

In the case of molecular dissociation, anisotropy of the fragments and thus the geometry of the molecules at the moment of dissociation has been of special interest.The measurements performed on ammonia, sulfur dioxide, water, ozone and nitrogen show clear evidence of anisotropy arising from alignment upon core excitation. This provides information on the symmetry of the core excited state as well as geometry changes. The anisotropy indirectly provides information on localization/delocalization of the core excitation. Oxygen $1s$ to "sigma like" transitions show clear evidence for localized excitation in ozone but not in sulfur dioxide.

Moreover the spectrometer is used to perform multi-coincidence studies of dynamic effects of argon cluster fragmentation. Both size and energy dependent measurements are reported. Evidence for nuclear rearrangements before fragmentation is found for small ($<$N$>\sim 5$) argon clusters by studying the fragmentation patterns around the argon $2p$ threshold. The time frame of dissociation for various cluster sizes is also presented. This in connection with a model describing the influence on the peaks shapes for dissociation on a picosecond to microsecond time scale in the spectrometer.

**Keywords:** *fragmentation, dissociation, mass spectroscopy, core excitation, molecules, clusters, induced alignment, electron-ion coincidence, localized excitation, synchrotron radiation, photoionization*

# Preface

The experimental work was performed at beam-line I411 at the MAX-lab synchrotron radiation facility, Lund University, Sweden, with two exceptions: papers II and V, where the experimental part was performed at Laboratório Nacional de Luz Síncroton (LNLS) in Campinas, Brazil.

The first part provides an introduction to the research field together with a description of the models and equipment used. The results are reported in the following papers constituting the second half of the thesis.

I *Molecular alignment of ammonia studied by electron-ion-ion coincidence spectroscopy*
**A. Lindgren**, M. Gisselbrecht, F. Burmeister, A. Naves de Brito, A. Kivimäki and S. L. Sorensen
J. Chem. Phys. **122** (2005) 114306

II *Core-Excited Electronic States and Fragmentation of Ozone – Analytic Tools and Experiment*
K. Wiesner, **A. Lindgren**, O. Björneholm, F. Burmeister, R. R. T. Marinho, A. Mocellin, L. Rosenqvist, S. L. Sorensen and A. Naves de Brito
Submitted to J. Chem. Phys. (2006)

III *Absence of symmetry breaking observed for* O $1s$ *core-excited sulfur dioxide*
**A. Lindgren**, N. Kosugi, M. Gisselbrecht, A. Kivimäki, F. Burmeister, A. Naves de Brito and S. L. Sorensen
Submitted to J. Chem. Phys. (2006)

IV *Resonant electron-ion coincidence measurements of water near the oxygen K-edge*
**A. Lindgren**, M. Gisselbrecht, S. Masuda, A. Kivimäki and S. L. Sorensen
To be submitted to Chem. Phys. (2006)

V *Description and performance of an electron-ion coincidence TOF spectrometer used at the Brazilian synchrotron facility LNLS*
F. Burmeister, L. H. Coutinho, R. R. T. Marinho, M. G. P. Homem, M. A. A. de Morais, A. Mocellin, O. Björneholm, S. L. Sorensen, P. T. Fonseca, **A. Lindgren** and A. Naves de Brito
To appear in J. Electron Spectrosc. Relat. Phenom. (2006)

VI *Photon energy dependence of fragmentation of small argon clusters*
M. Gisselbrecht, **A. Lindgren**, M. Tchaplyguine, F. Burmeister, G. Öhrwall, M. Lundwall, M. Lundin, R. R. T Marinho, A. Naves de Brito, S. Svensson, O. Björneholm and S. L. Sorensen
J. Chem. Phys. **123** (2005) 194301

VII *Size dependence fragmentation of argon clusters*
M. Gisselbrecht, **A. Lindgren**, M. Tchaplyguine, F. Burmeister, G. Öhrwall, M. Lundin, A. Naves de Brito, S. Svensson, O. Björneholm and S. L. Sorensen
To be submitted (2006)

**Comments on my own contribution to the papers**

In all papers listed above I have contributed significantly to the work. For all papers where I am the first author I have, in addition to being highly involved in the measurements, been responsible for the analysis of the data as well as for the writing of the paper. For the papers where I am not the first author, my contribution is reflected by the position in the author list. In papers II and V my main contribution have been the development of the simulations and the calculation of the PIPICO profiles and the discussion concerning the interpretation of the data, but I have not been involved in the measurements.

**List of papers not included in the dissertation, to which I have contributed**

i *Radial surface segregation in free heterogeneous argon/krypton clusters*
M. Lundwall, M. Tchaplyguine, G. Öhrwall, R. Feifel, A. Lindblad, **A. Lindgren**, S. L. Sorensen, S. Svensson, O. Björneholm
Chem. Phys. Lett. **392** (2004) 433-438

ii *Observation of elastic scattering effects on photoelectron angular distributions in free Xe clusters*
G. Öhrwall, M. Tchaplyguine, M. Gisselbrecht, M. Lundwall, R. Feifel, T. Rander, J. Schulz, R. R. T. Marinho, **A. Lindgren**, S. L. Sorensen, S. Svensson and O. Björneholm
J. Phys. B **36** (2003) 3937

# Acknowledgements

I would like to adress gratitude to my supervisor Stacey for guiding me in the molecular science field. I am also very obliged to Mathieu who has helped me a lot on how to perform experiments, find my way at MAX-lab and ”how to survive in the academic world”. Thanks for encouraging me to carry on.

Past and present people working in Uppsala also deserve my appreciation: Denis (thanks for the Paris trip), Karoline (I am grateful for all the help on the peak-shape profiles as well for all discussions), Florian, Marcus, Ingela, Andreas, Torbjörn, Gunnar, Olle and Svante.

Arnaldo, Antti and Reinhold, thanks for sharing your vast knowledge.

Suomi, I am thankful for all the discussions during the finishing work of my thesis.

Many thoughts go to Johan, thank you for being a great roommate during these years, and keeping up the good work of sustaining the neverending chaos in the office. I have missed you since you ended you Ph.D studies. I would also like to acknowledge all my other roommates, past and present. Andrea, Emelie, Jessica, Rasmus, Lassana and Henrik thanks for the chats when one does not feel like doing something serious.

The co-workers, past and present, at the department deserves my acknowledgement.

All the staff at MAX-lab. Thanks!!! Especially Magnus (for all the help with computers and electronics), Micke (it is always nice to have a chat about something not concerning science, like guitars or karate), Maxim and Joachim (for all help at the beamline), Stefan, Kurt and Anders (for all the help with various experimental things) and Helena (for all the small chats).

I adress my appreciation to Carl-Erik for encouraging me to start my Ph. D. studies.

A big Thank you! to all students and co-teachers I have met during my time teaching at Kurslab, the times in the classroom is by far the most valuable time.

I would also like to adress my gratitude to some artists that have inspired me a lot throughout this years. To mention some: Metallica, Entombed, Opeth, Kent, Silverbullit, the Soundtrack of our lives, the Hellacoptes, Isis, bob hund, Oasis....

Many thoughts go to my family and friends for being there for me in good times, and in bad. Mamma, Pappa, Karin, Daniel, Göran, Lina, Henrik, Martin, Anil, Linnea, Ulrika, Kerstin, Alfons, Amanda, Sara and Emil. Thanks!!!

Linda, living in your home during the last weeks of completing this work did help me a lot. Kiss, kiss my darling!

Cheers!!!

# Contents

Chapter 1

# Introduction

The aim of this thesis is to study fragmentation dynamics for molecules and clusters by coincidence ion spectroscopic methods.

For molecules fragmentation studies measuring electron ion coincidences is a well known technique. The PhotoElectron-PhotoIon$^{X}$-COincidence (PE(PI)$^{X}$CO), where X is the number of coincident ions measured) was introduced by Eland *et al.* [1] and Frasinski *et al.* [2] in 1986 for the valence energy region and further developed by Morin *et al.* [3] for the inner-shell energy region. The main aim for the groups of Eland, Fransinski and Morin was to understand the branching ratios of different fragmentation channels and the dynamics of fragmentation i.e. if the process is sequential or instantaneous. Hanson *et al.* [4] developed the technique detecting energy resolved electrons in order to connect fragmentation to specific electronic states in the inner-shell energy region. Since then many groups joined the development. A large branch is the use od Threshold-PhotoElectron-Photoion COincidence (TPEPICO) spectroscopy for mapping the valence energy region.

The interest of aligned molecules after core excitation started by the group of Saito *et al.*. They used the PE(PI)$^{X}$CO technique to describe the anisotropic distribution of the ionic fragments described by the so-called $\beta$-value [5]. Another method using ion yield measurements probing anisotropy was developed by Shigemasa *et al.*. Whereas the PE(PI)$^{X}$CO technique is based on mass spectroscopy collecting all ions, the ion yield measurement measures only the number of ions emitted in different directions. Both groups concentrated on measurements of diatomic molecules where the findings mostly confirmed the expected anisotropy. However results from measurements on Rydberg states on CO showed a clear discrepancy. This was explained by the anisotropy of the slowly dissociative $CO^{2+}$ states which have time to rotate before dissociation [6]. Since then the effect of isotropic distributions of low-energy ions has been observed in several cases.

For polyatomic molecules geometry changes of the molecule before or during the dissociation have been seen as a "disturbance" in the anisotropy parameter as discussed and analyzed by Kosugi *et al.* [7]. Ground-state linear triatomic molecules can have both linear and bent core excited states. The fragment ions may then have rather large momenta orthogonal to the original molecular axis if the fragmentation takes place during the bending motion, which normally has the same time frame (fs) as the dissociation. The group of Ueda *et al.* combined the techniques of anisotropic detection of ionic fragments and energy analyzed electrons in order to study dissociation dynamics and geometry changes of core excited molecules in dif-

ferent states [8].

To further map geometry changes of molecules in different core-excited states, the ion coincidence technique was developed towards multiple-ion coincidence momentum imaging. Two main branches of measurements is used; 2D momentum imaging (velocity mapping) and 3D momentum imaging. In the 2D momentum imaging the distribution in energy and angles of the particles are measured whereas the 3D momentum imaging measures the energy and angle of emission for each particle. Examples are the studies of the bent and linear geometries of the excited states in triatomic linear molecules such as $CO_2$ and $N_2O$ [9, 10, 11, 12, 13]. Also asymmetric nuclear motion in $BF_3$ has been reported [14].

In light of this our aim was to develop the "simple" electron ion coincidence technique further together with models in order to get a more complete picture of the induced molecular alignment after core excitation without the need of "complex" multiple ion coincidence momentum imaging techniques. This requires very high quality data, where the details of peak shapes are crucial. The key point in our treatment is the induced alignment after core excitation and the preservation of it before dissociation. This is found valid in many measurements before as discussed above. A clear sign of alignment is the anisotropy seen in the spectra, the molecule has no time to rotate before dissociation. Eventual vibration will be seen as change in the geometry of the molecule at the moment of dissociation. With this in mind, models describing the symmetry properties of the core excited states as well as dynamical processes of the dissociation are deduced and presented in this thesis. From the models, information on the molecular bond angle, the kinetic energy released, sequential or concerted dissociation and momentum distribution to the fragments can be found.

Clusters are interesting to study in order to get more information on the evolution of material properties, from atomic/molecular size to infinite solid. To contribute to this understanding we performed ion coincidence spectroscopic measurements on argon clusters. Little quantitative work on cluster fragmentation exists, outside the work of the groups of Haberland *et al.*, Rühl *et al.* and Stace *et al.*. For small clusters we found that the fragmentation processes were sensitive to resonant and non resonant excitations. Another study aimed at understanding the cluster size dependence on fragmentation, we could clearly see traces of molecular dissociation in small clusters, but for clusters larger than 100 atoms another model is needed. In the long run the aim is to study how energy dissipate when it from the beginning is localized on a surface or bulk atom in the cluster.

Although the research presented here is considered to be fundamental research the understanding of the interaction between radiation and matter play an important role in a wide variety of fields. To mention some; environmental science (how does radiation from the sun interact with the atmosphere? e.g. ozone production and dissociation), energy production (how can we produce better solar cells?) medicine (how can we treat cancer?).....

The outline of the text is as follows. I present some key issues in the properties of photoabsorbtion and the relaxation processes for both molecules and clusters. A description of the spectrometer follows before continuing with a presentation of the methods and models used for the data analysis. Last but not least the results presented in the papers are summarized.

Enjoy the reading!

Chapter 2

# Molecules

When combining two or more atoms into a new unit the new particle is called a *molecule*. The name has it's origin in the Latin word *molecula* "small mass" and the concept of molecules was first introduced in 1811 by Avogadro. A more precise definition of a molecule is the smallest unit of a substance which exhibits all of its chemical and physical properties. According to the strict definition, molecules can consist of one atom (as in noble gases) or of several atoms bonded together. In molecular sciences though, a molecule consists of two or more atoms. The simplest molecules in this sense are diatomic and homonuclear; made up of two atoms of the same kind, e.g. $H_2$, $O_2$ or $N_2$. The next simplest group is molecules consisting of two atoms of different kind, so called heteronuclear diatomic molecules, e.g. CO, HCl or NO. Combining more than two atoms the molecules can have different geometrical structures, e.g. a triatomic molecule can be linear or bent by different angles. The geometry is determined by the nature of the chemical bonds by which it is connected to its neighboring atoms and can be described by the bond lengths of two joined atoms, bond angles of three connected atoms, and torsion angles of three consecutive bonds.

Molecules are most often held together with covalent bonds involving single, double, and/or triple bonds, where a "bond" is a shared pair of electrons. The sharing of one or more pairs of electrons between two components, producing a mutual attraction that holds the resultant molecule together. Atoms tend to share electrons in such a way that their outer electron shells are filled. The idea of covalent bonding was introduced by Gilbert N. Lewis in 1916 when he introduced the so called 'Lewis Notation' or 'Electron Dot Notation' (EDN) in which valence electrons (those in the outer shell) are represented as dots around the atomic symbols. Pairs of electrons located between atoms represent covalent bonds. Multiple pairs represent multiple bonds, such as double and triple bonds. Some examples of EDN are shown in Fig. 2.1. Some structures can have more than one valid EDN, e.g. ozone. In a diagram of ozone the center atom will have a single bond with one atom and a double bond with the other. The diagram cannot tell us which atom has the double bond; either of the terminal atoms have equal chances of having the double bond. In reality the bond property is delocalized. Instead of having one double bond and one single bond, there are actually two "1.5 bonds" with approximately three electrons in each at all times. This is pictured as an arc in the alternative notation.

While the idea of shared electron pairs provides an effective qualitative picture of covalent bonding, quantum mechanics is needed to understand the nature of these bonds and predict

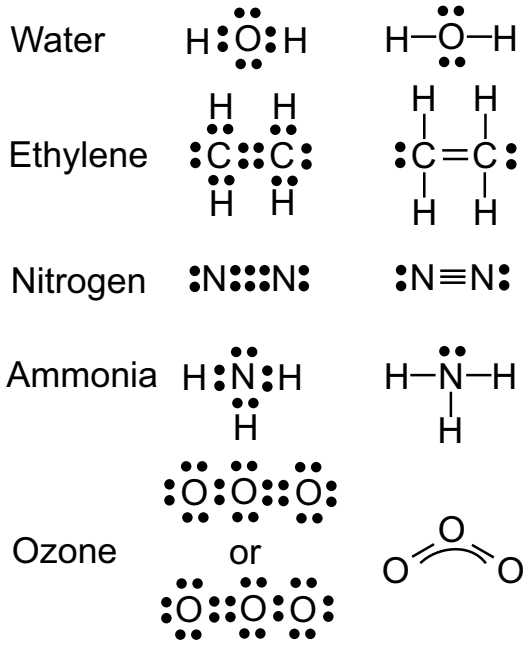


**Figure 2.1**: Some examples of the 'Electron Dot Notation' for covalent bonds. An alternative form, in which bond-forming electron pairs are represented as solid lines, is shown alongside. Usually the electrons not included in the bond are neglected in the representations to the right, but are included here for clarification.

the geometrical structures and properties of simple molecules. Historically this was based on the valence bond model, which assumes that a chemical bond is formed when there is constructive overlap between the atomic orbitals of participating atoms. These atomic orbitals are known to have specific angular relationships between each other, and thus the valence bond model can successfully predict the bond angles observed in simple molecules. Today the valence bond model has been supplemented with the molecular orbital model. In this model the molecular orbitals are formed as linear combinations of atomic orbitals.

The covalent bond can be divided into two different types; $\sigma$ and $\pi$ bonds. In $\sigma$ bonds a single lobe of one involved electron orbital overlaps a single lobe of the other involved electron orbital. The orbital has no node planes between the two atoms. $\sigma$ bonds are the strongest type of covalent bonds; the most intense parts of the involved electron orbitals overlap. The Greek letter $\sigma$ in their name refers to atomic $s$ orbitals, since the orbital symmetry of the $\sigma$ bond is the same as that of the $s$ orbital when seen down the bond axis. The simplest $\sigma$ bond is between the two $s$ orbitals in molecular hydrogen but e.g. also two overlapping $p$-type orbitals can form a $\sigma$ bond, see Fig. 2.2.

In $\pi$ bonds two lobes of one involved electron orbital overlap two lobes of the other involved electron orbital, Fig. 2.2. The Greek letter $\pi$ in their name refers to $p$ orbitals, since the orbital symmetry of the $\pi$ bond is the same as that of the $p$ orbital when seen down the bond axis. $\pi$ bonds are usually weaker than $\sigma$ bonds because their orbitals go further from the positive charge of the atomic nucleus, which requires more energy. From the perspective of quantum mechanics, this bond weakness is explained by significantly less overlap between the previously $p$-orbitals due to their parallel orientation.

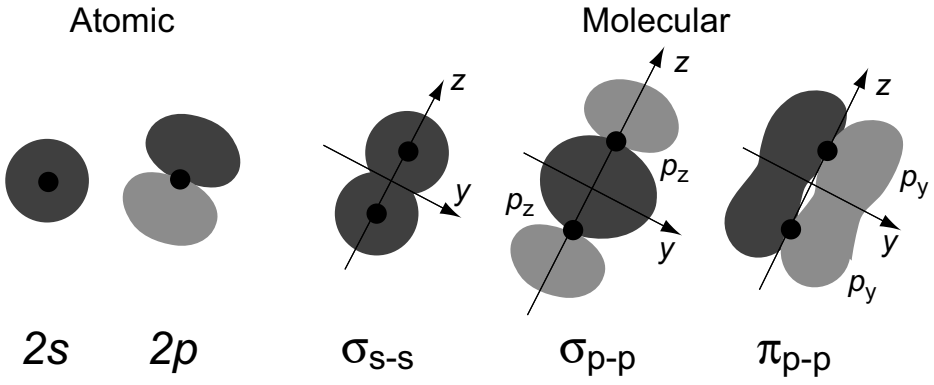


**Figure 2.2**: A descriptive picture of the atomic $s$ and $p$ orbitals as well as the $\sigma$ and $\pi$ bonds.

## 2.1 Molecular Orbitals

Molecular orbitals are built up essentially of linear combinations of atomic orbitals (LCAO) from the constituent atoms. The molecular orbitals are constructed according to specific constraints arising mainly from energy and symmetry considerations as well as overlap between the atomic orbitals used. As these properties, especially the symmetry properties of different molecular states, are central to the experiments in this thesis, a presentation of molecular orbitals is given. The treatment will be limited to molecules consisting of low-Z atoms, e.g. H, C, N, O and F.

The $1s$ electrons of H and/or the $2s$ and $2p$ electrons of the periodic table second row atoms have binding energies in the same energy range this means that one of the properties to form molecular orbitals are fulfilled. Another property of importance is that the atomic orbitals shall overlap. An example of this is $N_2$ where the $2s$ and $2p$ orbitals overlap whereas the $1s$ orbitals do not (the $1s$ atomic orbitals in $N_2$ are located to close to the nuclei, resulting in a negligible overlap). The last property to be fulfilled is that the atomic orbitals shall have the same kind of symmetry. A good way to describe the symmetry properties of molecular orbitals is to use group theory and designate the molecular orbitals by their irreducible representations.

### 2.1.1 Symmetry Properties and Irreducible Representations

The symmetry properties used to construct molecular orbitals are presented in the irreducible representations found in the character tables for the appropriate point group. The convention used in the literature is used here, where the principal symmetry axis of the molecule is taken as the $z$-axis and capital Roman letters are used for the irreducible representations of the point groups and lower-case italic letters for the labelling of the orbitals.

Lets consider the case of a heteronuclear diatomic molecule, e.g. CO or HF. These kinds of molecules have $C_{\infty v}$ symmetry and from the character table of this point group (Table 2.1) one finds that the $\Sigma$ representation transforms like $z$ and therefore characterizes the symmetry properties of the $2p_z$ orbital. The spherically symmetric $2s$ atomic orbital is represented by the function $x^2 + y^2 + z^2$, which also transforms as $\Sigma$. In contrast, the $2p_x$ and $2p_y$ atomic

**Table 2.1**: Character tables for some different symmetry representations.

| $C_s$ | $E$ | $\sigma_h(yz)$ | Linear func. and rotations | Quadratic func. |
|---|---|---|---|---|
| A′ | 1 | 1 | $(x, y)\boldsymbol{R}_z$ | $x^2$,$y^2$,$z^2$,$xy$ |
| A″ | 1 | -1 | $z(\boldsymbol{R}_x, \boldsymbol{R}_y)$ | $(xz, yz)$ |

| $C_{\infty v}$ | $E$ | $2C_\infty^\phi$ | $\cdots$ | $\infty\sigma_v$ | Linear func. and rotations | Quadratic func. |
|---|---|---|---|---|---|---|
| $\Sigma$ | 1 | 1 | $\cdots$ | 1 | $z$ | $x^2 + y^2 + z^2$ |
| $\Pi$ | 2 | $2\cos\phi$ | $\cdots$ | 0 | $(x, y)(\boldsymbol{R}_x, \boldsymbol{R}_y)$ | $(xz, yz)$ |

| $C_{2v}$ | $E$ | $C_2$ | $\sigma_v(xz)$ | $\sigma'_v(yz)$ | Linear func. and rotations | Quadratic func. |
|---|---|---|---|---|---|---|
| $A_1$ | 1 | 1 | 1 | 1 | $z$ | $x^2, y^2, z^2$ |
| $A_2$ | 1 | 1 | -1 | -1 | $\boldsymbol{R}_z$ | $xy$ |
| $B_1$ | 1 | -1 | 1 | -1 | $x, \boldsymbol{R}_y$ | $xz$ |
| $B_2$ | 1 | -1 | -1 | 1 | $y, \boldsymbol{R}_x$ | $yz$ |

| $C_{3v}$ | $E$ | $2C_3$ | $3\sigma_v$ | Linear func. and rotations | Quadratic func. |
|---|---|---|---|---|---|
| $A_1$ | 1 | 1 | 1 | $z$ | $x^2 + y^2, z^2$ |
| $A_2$ | 1 | 1 | -1 | $\boldsymbol{R}_z$ | |
| E | 2 | -1 | 0 | $(x, y)(\boldsymbol{R}_x, \boldsymbol{R}_y)$ | $(x^2 - y^2, xy)(xz, yz)$ |

orbitals, associated with the functions $x$ and $y$, transform as the $\Pi$ representation. Applying the most important rule in constructing molecular orbitals, that only orbitals belonging to the same irreducible representation (having the same symmetry) can mix, the $2s$ and $2p_z$ orbitals in a $C_{\infty v}$ molecule can mix and form $\sigma$ orbitals. The $2p_x$ and $2p_y$ on the other hand have $\Pi$ symmetry and form $\pi$ orbitals, see Fig. 2.2.

Next we consider bent triatomic molecules with the same kind of terminal atoms, e.g. $H_2O$, $SO_2$ and $O_3$. Molecules of this kind belong to the $C_{2v}$ symmetry group. Again the $z$-axis is chosen to be along the principal symmetry axis of the molecule, see top of Fig. 2.3. In this case it is a so called $C_2$ axis (by rotate half a turn along the z-axis the result look the same as the starting point). The index v is used since there are two vertical symmetry planes (vertical because the principal symmetry axis is laying in the vertical plane). Continuing building the coordinate system to describe the $C_{2v}$-molecules we choose the $x$-axis to be perpendicular to the molecular plane (an alternative coordinate system with the $y$-axis perpendicular to the molecular plane can also be found in the literature). Looking in the character table for the $C_{2v}$ symmetry group (Table 2.1) the $1s$, $2s$ and $2p_z$ orbitals transform like the $A_1$, the $2p_x$ orbital like the $B_1$ and the $2p_y$ orbital like the $B_2$ irreducible representations. In water the localized oxygen $1s$ orbital is given the $1a_1$ label. Mixing the $2s$ and $2p_z$ orbitals with the appropriate symmetry adapted pairs of hydrogen orbitals results in the $2a_1$, $3a_1$ and $4a_1^*$ molecular orbitals. The oxygen $2p_x$ orbital form the $1b_1$ molecular orbital and the oxygen $2p_y$ together with hydrogen orbitals forms the $1b_2$ and $2b_2^*$ molecular orbitals. In Figure 2.3 a schematic picture of the molecular orbitals and the molecular coordinate system for $H_2O$ is shown.

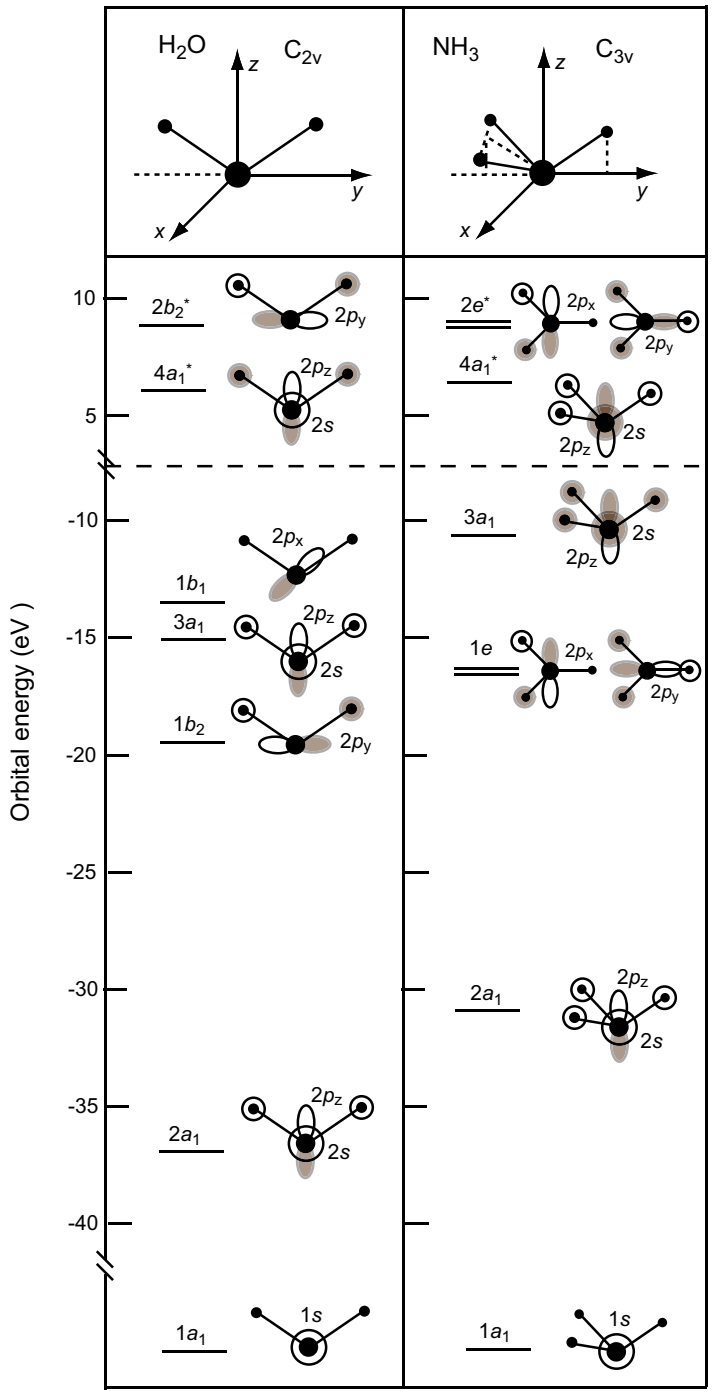


**Figure 2.3**: A sketch of the atomic orbital composition for the molecular orbitals in water and ammonia together with a coordinate system for each molecule. The molecular orbitals are labeled by their irreducible representation, see the text. Note that the irreducible representations $b_1$ and $b_2$ for $H_2O$ depend on the choice of the $x$- and $y$-axes. The figure is made with help from Fig. 3.3 in [15].

Pyramidal molecules such as ammonia have $C_{3v}$ symmetry (a $C_3$ axis as the main symmetry axis and three vertical symmetry planes). For ammonia the nitrogen $1s$ orbital is denoted as the $1a_1$ molecular orbital because it has $A_1$ symmetry (Table 2.1). Again the mixing of $2s$ and $2p_z$ orbitals, corresponding to the $A_1$ irreducible representation, together with hydrogen orbitals leads to the $2a_1$, $3a_1$ and $4a_1^*$ molecular orbitals. The $2p_x$ and $2p_y$ orbitals correspond to the E irreducible representation and forms together with hydrogen orbitals the $1e$ and $2e^*$ molecular orbitals. A sketch of the molecular orbitals is found in Figure 2.3.

## 2.2 Photoabsorption

Ionization of an atom or a molecule can occur if enough energy is absorbed. The minimum energy required is called the single ionization potential. According to Koopman's theorem, [16], the single ionization potential is equal to the orbital energy of the least bound electron, which is on the order of a few eV. Of course even more deeply bound electrons can be ejected if the energy is high enough. Energy conservation gives the relation:

$$h\nu = E_{\text{kin}} + E_{\text{f}} - E_{\text{i}} \tag{2.1}$$

where $h\nu$ is the photon energy, $E_{\text{kin}}$ the kinetic energy of the outgoing electron, $E_{\text{f}}$ the energy of the final ionized system and $E_{\text{i}}$ the energy of the initial neutral system. By measuring the kinetic energy of the outgoing electron as a function of photon energy, information on the electronic structure can be obtained. This is the basis of photoelectron spectroscopy. Note that the ionization cross section decreases for a specific orbital as the photon energy is increased sufficiently above its ionization potential.

The system can also absorb a discrete amount of energy taking an electron from an occupied orbital to a non-filled or empty orbital and form a short-lived (usually) neutral state. These kind of states are called excited states. For molecules there are mainly two types of excited states formed, valence type and Rydberg type. In the valence type states the orbital is described by using the molecular orbital picture given in section 2.1 and thus there is a strong correlation between the molecule's ionic core and the electron in that orbital. In Rydberg states the excited electron can be treated as seeing the nucleus and the other electrons as one singly charged particle, here the electron is decoupled from the description of the rest of the molecule. One treats the electron by itself and treats the rest of the molecule as ionic.

## 2.3 Transitions and Selection Rules

The electronic transition probability between an initial state and a final state within the dipole approximation can be expressed (see e.g. [15, 17, 18]):

$$P_{\text{if}} \propto |\mathbf{e}\cdot < \text{f} \mid \mathbf{r} \mid \text{i} > |^2 \tag{2.2}$$

where $\mathbf{r}$ is the position vector for the electrons and assuming the exciting radiation to be linearly polarized in the direction of the unit vector $\mathbf{e}$. This thesis will deal with electronic transitions where an electron is promoted from a core orbital into an empty or non-filled valence or Rydberg orbital. Let us evaluate the dipole matrix element $< \text{f} \mid \mathbf{r} \mid \text{i} >$ in eqn (2.2) from an initial $1s$ state in a molecule consistent of low-Z atoms. The initial state

$\mid$ i $>= R_{1s}(r)$ is spherically symmetric and is to a very good approximation represented by the atomic $1s$ wavefunction of the excited atom in the molecule. The final state in the transition can be described by a LCAO wavefunction of the corresponding molecular orbital and because of the localization of the $1s$ state, the atomic valence components of the excited atom dominate. Thus, for low-Z atoms, the final state wavefunction can be expressed:

$$\begin{aligned} \mid \mathrm{f} > &= a \mid 2s > +b \mid 2p_{\mathrm{x}} > +c \mid 2p_{\mathrm{y}} > +c \mid 2p_{\mathrm{z}} > \\ &= aR_{2\mathrm{s}}(r) + R_{2\mathrm{p}}(r)(b\sin\theta\cos\phi + c\sin\theta\sin\phi + d\cos\theta) \end{aligned} \tag{2.3}$$

where the coefficients $a$, $b$, $c$ and $d$ give the weight of the atomic orbitals in the LCAO expansion, and $R_{2\mathrm{s}}(r)$ and $R_{2\mathrm{p}}(r)$ are the radial atomic wavefunctions. By expressing the electron position vector in spherical coordinates

$$\mathbf{r} = r(\sin\theta\cos\phi e_{\mathrm{x}} + \sin\theta\sin\phi e_{\mathrm{y}} + \cos\theta e_{\mathrm{z}}), \tag{2.4}$$

where $e_{\mathrm{i}}$ are the direction of the unit vector, the dipole matrix element in 2.2 can be evaluated. We obtain

$$< \mathrm{f} \mid \mathbf{r} \mid \mathrm{i} >= R\frac{4\pi}{3}(be_{\mathrm{x}} + ce_{\mathrm{y}} + de_{\mathrm{z}}) = R\frac{4\pi}{3}\mathbf{O} \tag{2.5}$$

where $R$ is the radial dipole matrix element

$$R = \int R_{1\mathrm{s}}(r)R_{2\mathrm{p}}(r)r^3\mathrm{d}r \tag{2.6}$$

and $\mathbf{O}$ is the direction of the largest amplitude of the final state orbital. Thus for $K$-shell excitation the transition dipole moment points in the same direction as the $p$-component in the final state orbital on the excited atom. The transition probability can now be expressed:

$$P_{\mathrm{if}} \propto |\mathbf{e}\cdot < \mathrm{f} \mid \mathbf{r} \mid \mathrm{i} > |^2 \propto| \mathbf{e}\cdot\mathbf{O} \mid^2 . \tag{2.7}$$

This shows that the transition probability is strongly dependant on the direction of the polarization of the radiation driving the transition relative the molecular transition dipole moment.

Let us now look at a simple example: $K$-shell transitions to the $\sigma^*$ or to the $\pi^*$ orbitals in diatomic molecules, e.g. CO or $N_2$. First we must orient our coordinate system so that the internuclear axis, and therefore the $\sigma^*$ orbital, lies along the $z$-axis, and the two degenerate $\pi^*$ orbitals lie along the $x$ and $y$-axes. We also specify the orientation of the unit electric field vector $\mathbf{e}$ by the spherical angles $\theta'$ and $\phi'$. Now the polarization dependence of the dipole transition probability to a $\sigma^*$ or $\pi^*$-type molecular orbital is given by

$$P_{\mathrm{if}}(\sigma) \propto \mid \mathbf{e}\cdot\mathbf{e}_{\mathrm{z}} \mid^2 \propto \cos^2\theta' \tag{2.8a}$$

$$P_{\mathrm{if}}(\pi) \propto \mid \mathbf{e}\cdot\mathbf{e}_{\mathrm{x}} \mid^2 + \mid \mathbf{e}\cdot\mathbf{e}_{\mathrm{y}} \mid^2 \propto \sin^2\theta'\cos^2\phi' + \sin^2\theta'\sin^2\phi' = \sin^2\theta'. \tag{2.8b}$$

Thus the $\sigma^*$ transition probability is greatest for the linear polarization vector along the internuclear axis and vanishes when it is perpendicular and the $\pi^*$ transition probability shows the opposite behavior. This is the foundation of the alignment effect discussed in section 2.4.2.

Until now we have assumed that $K$-shell excitation occurs on a particular atom due to spatial localization of the $1s$ initial state. Thus it is the local symmetry of the molecular final state orbital on the excited atom which determines whether the transition is allowed or forbidden. E.g. for $1s$ initial states the final state must have a $p$ orbital component; the

angular momentum must change by 1. To be able to decide if a transition is allowed or not a very useful method is to use group theory by looking on the symmetry properties. But before examining this approach further we examine different ways of considering the effect of the core hole localization. Does the localization affect the symmetry of the initial and final states? Shall we treat the final state as being of the same symmetry as the initial state?

### 2.3.1 Preserved or Broken Symmetry

One approach is to say that the symmetry of the final state is broken because the delocalization ability in the valence electron is weaker than the localization effect of the core electron. The broken symmetry is obtained from the ground state symmetry by assuming that the excited atom is changed by its core hole and as such is different from the other atoms of the same species in the molecule. In this case the $1s$ initial state transforms like the totally symmetric representation of the broken symmetry point group and the selection rules for the allowed transitions are worked out using the broken symmetry point group. Another approach is to treat the core hole as if it is delocalized. In this case the $1s$ initial state corresponds to the irreducible representation which describes the possible delocalized hole combination in the full symmetry of the molecular ground state. Thus the selection rules are worked out in this symmetry. However, strictly speaking, the correct approach is to consider the whole set of broken symmetry configurations and form linear combinations thereof such that the transition can take place within the higher symmetry of the ground state.

In practice the three procedures usually arrive at the same result [19]. Though the delocalized molecular orbital picture, using the symmetry of the molecular ground state, is generally more convenient in the discussion of dipole electronic transitions. But sometimes the latter approach is needed in order to describe the system more correctly, e.g. transitions from the terminal $1s$ levels in bent triatomic molecules of the form XYX (see below).

### 2.3.2 Applications of the Group Theoretical Selection Rules

For the electronic transition to be allowed, the dipole matrix element integral in eq. (2.2) must be non zero. An elegant way to check this is to use group theory. For the integral $< \mathrm{f} \mid \mathbf{r} \mid \mathrm{i} >$ to be non zero, the integrand must span the totally symmetric species of the point group considered, e.g. in $C_{3v}$ it should span $A_1$ and in $C_{\infty v}$ is should span $\Sigma$ [15, 17, 18].

#### Pyramidal Molecules-Central Core Transitions

For $1s$ transitions from the central atom in pyramidal molecules, e.g. N $1s$ transitions in ammonia, the core hole localization does not reduce the symmetry. Thus we simply consider the transition selection rules for the molecular ground state, namely $C_{3v}$. A convenient way is to examine all three components of the dipole matrix element separately. Because the initial state is a closed shell with $A_1$ symmetry, we will limit the treatment to transitions where the initial state can be described as having $A_1$ symmetry, starting with transitions to a state with the same symmetry and then continue with transitions to states with the other two symmetry possibilities $A_2$ and E.

From Table 2.2 (a) we find that only the $z$-component of the dipole matrix element spans the totally symmetric species $A_1$, thus an $A_1$ to $A_1$ transition is allowed and has its maximum

**Table 2.2**: The table is used to find out if the transition from an initial state ($\psi_\mathrm{i}$) to a final state ($\psi_\mathrm{f}$) belonging to the $C_{3v}$ symmetry group is allowed or forbidden. One must examine all three components of the transition dipole moment separately. The result can be found in the last row. For the transition to be allowed the product $\psi_\mathrm{f}\mathbf{r}\psi_\mathrm{i}$ must span the totally symmetric irreducible representation, $A_1$ in this case.

(a)

| | | $x$-component | | | | $y$-component | | | | $z$-component | | | |
|---|---|---|---|---|---|---|---|---|---|---|---|---|---|
| | | $E$ | $2C_3$ | $3\sigma_\mathrm{v}$ | | $E$ | $2C_3$ | $3\sigma_\mathrm{v}$ | | $E$ | $2C_3$ | $3\sigma_\mathrm{v}$ | |
| $\psi_\mathrm{f}$ | $A_1$ | 1 | 1 | 1 | | 1 | 1 | 1 | | 1 | 1 | 1 | |
| $\mathbf{r}$ | | 2 | -1 | 0 | | 2 | -1 | 0 | | 1 | 1 | 1 | |
| $\psi_\mathrm{i}$ | $A_1$ | 1 | 1 | 1 | | 1 | 1 | 1 | | 1 | 1 | 1 | |
| $\psi_\mathrm{f}\mathbf{r}\psi_\mathrm{i}$ | | 2 | -1 | 0 | $\Rightarrow$E | 2 | -1 | 0 | $\Rightarrow$E | 1 | 1 | 1 | $\Rightarrow A_1$ |

(b)

| | | $x$-component | | | | $y$-component | | | |
|---|---|---|---|---|---|---|---|---|---|
| | | $E$ | $2C_3$ | $3\sigma_\mathrm{v}$ | | $E$ | $2C_3$ | $3\sigma_\mathrm{v}$ | |
| $\psi_\mathrm{f}$ | $A_1$ | 1 | 1 | 1 | | 1 | 1 | 1 | |
| $\mathbf{r}$ | | 2 | -1 | 0 | | 2 | -1 | 0 | |
| $\psi_\mathrm{f}$ | E | 2 | -1 | 0 | | 2 | -1 | 0 | |
| $\psi_\mathrm{f}\mathbf{r}\psi_\mathrm{i}$ | | 4 | -1 | 0 | $\Rightarrow A_1+A_2+E$ | 4 | -1 | 0 | $\Rightarrow A_1+A_2+E$ |

| | | $z$-component | | | |
|---|---|---|---|---|---|
| | | $E$ | $2C_3$ | $3\sigma_\mathrm{v}$ | |
| $\psi_\mathrm{i}$ | $A_1$ | 1 | 1 | 1 | |
| $\mathbf{r}$ | | 1 | 1 | 1 | |
| $\psi_\mathrm{f}$ | E | 2 | -1 | 0 | |
| $\psi_\mathrm{f}\mathbf{r}\psi_\mathrm{i}$ | | 2 | -1 | 0 | $\Rightarrow$E |

(c)

| | | $x$-component | | | | $y$-component | | | | $z$-component | | | |
|---|---|---|---|---|---|---|---|---|---|---|---|---|---|
| | | $E$ | $2C_3$ | $3\sigma_\mathrm{v}$ | | $E$ | $2C_3$ | $3\sigma_\mathrm{v}$ | | $E$ | $2C_3$ | $3\sigma_\mathrm{v}$ | |
| $\psi_\mathrm{i}$ | $A_1$ | 1 | 1 | 1 | | 1 | 1 | 1 | | 1 | 1 | 1 | |
| $\mathbf{r}$ | | 2 | -1 | 0 | | 2 | -1 | 0 | | 1 | 1 | 1 | |
| $\psi_\mathrm{f}$ | $A_2$ | 1 | 1 | -1 | | 1 | 1 | -1 | | 1 | 1 | -1 | |
| $\psi_\mathrm{f}\mathbf{r}\psi_\mathrm{i}$ | | 2 | -1 | 0 | $\Rightarrow$E | 2 | -1 | 0 | $\Rightarrow$E | 1 | 1 | -1 | $\Rightarrow A_2$ |

when the polarization-vector of the light is parallel to $z$. Table 2.2 (b) is used to investigate the transition from an $A_1$ state to an E state. Here we see that both the $x$ and $y$ components span $A_1$. A consequence of this is that the transition is allowed and has its maximum when the polarization-vector of the light is in the $x, y$ plane. From Table 2.2 (c) we see that a transition between an $A_1$ state and an $A_2$ state is dipole forbidden; there are no components that span $A_1$. Thus the $1a_1 \rightarrow 4a_1^*$ and $1a_1 \rightarrow 2e^*$ transitions (see Fig. 2.1) are allowed and are strongest when the light polarization vector is parallel with the molecular $z$-axis and in the molecular $x, y$-plane, respectively.

**Bent Triatomic Molecules**

We now examine the selection rules for a bent triatomic molecule, XYX.

Let us first disregard core-hole localization and consider the transitions in the ground state symmetry, $C_{2v}$. Here the states have $A_1$ (totally symmetric), $A_2$, $B_1$ or $B_2$ symmetry. By adapting the same method as used for the $C_{3v}$ symmetry group above, and only regarding transitions from initial states with $A_1$ symmetry, the following dipole matrix elements are found to be non-zero:

$$|< A_1 \mid z \mid A_1 >|^2 \tag{2.9a}$$
$$|< B_1 \mid x \mid A_1 >|^2 \tag{2.9b}$$
$$|< B_2 \mid y \mid A_1 >|^2 \, . \tag{2.9c}$$

Thus transitions to states of $A_2$ symmetry are dipole forbidden.

For singly excited states exciting from the central $1sa_1$-orbital the $A_1$ excited state is given by a $1sa_1 \rightarrow a_1^*$ transition, the $B_1$ excited state is given by a $1sa_1 \rightarrow b_1^*$ transition and the $B_2$ excited state is given by a $1sa_1 \rightarrow b_2^*$ transition. Here capital letters are used to show the symmetry of the states and small letters are used to show the symmetry of the electron. Thus the dipole allowed matrix elements giving the different final states can be reduced as follows:

$$< A_1 \mid z \mid A_1 > \Rightarrow < a_1^* \mid z \mid 1sa_1 > \tag{2.10a}$$
$$< B_1 \mid x \mid A_1 > \Rightarrow < b_1^* \mid x \mid 1sa_1 > \tag{2.10b}$$
$$< B_2 \mid y \mid A_1 > \Rightarrow < b_2^* \mid y \mid 1sa_1 > \, . \tag{2.10c}$$

For the terminal atoms the $1s$-orbitals can build molecular orbitals of gerade or ungerade type. The gerade combination forms an $a_1$ molecular orbital whereas the ungerade combination forms a $b_2$ molecular orbital. Now the $A_1$ excited state is given by a $1sa_1 \rightarrow a_1^*$ or $1sb_2 \rightarrow b_2^*$ transition, the $B_1$ excited state is given by a $1sa_1 \rightarrow b_1^*$ or $1sb_2 \rightarrow a_2^*$ transition and the $B_2$ excited state is given by a $1sa_1 \rightarrow b_2^*$ or $1sb_2 \rightarrow a_1^*$ transition. And thus the dipole allowed matrix elements giving the different excited states can be reduced as follows:

$$< A_1 \mid z \mid A_1 > \Rightarrow < a_1^* \mid z \mid 1sa_1 > \text{ or } < b_2^* \mid z \mid 1sb_2 > \tag{2.11a}$$
$$< B_1 \mid x \mid A_1 > \Rightarrow < b_1^* \mid x \mid 1sa_1 > \text{ or } < a_2^* \mid x \mid 1sb_2 > \tag{2.11b}$$
$$< B_2 \mid y \mid A_1 > \Rightarrow < b_2^* \mid y \mid 1sa_1 > \text{ or } < a_1^* \mid y \mid 1sb_2 > \, . \tag{2.11c}$$

From this we see that both $1s \rightarrow a_1^*$ and $1s \rightarrow b_2^*$ transitions have degenerate $A_1$ and $B_2$ states. Thus from symmetry considerations the transitions are strongest when the light polarization vector is parallel with the molecular $x, y$-plane.

If we instead treat the core hole as localized, excitation of the central atom does not reduce the symmetry and we get the same result as in eqn (2.10). On the other hand, excitation of a terminal atom results in a symmetry reduction to $C_s$ [19]. The $A_1$ and $B_2$ representations in $C_{2v}$ correspond to the A′ representation in $C_s$ and the $B_1$ and $A_2$ representations in $C_{2v}$ correspond to the A″ representation in $C_s$, Table 60 in [20].

Consider transitions from a terminal $1s$ orbital into a $b_1^*$ molecular orbital. In the broken symmetry this corresponds to an $a' \rightarrow a''$ transition. Application of a linear combination of the broken symmetry configuration yields, within the $C_{2v}$ point group, two final states of $A_2$ and $B_2$ symmetry for this transition. Therefore, excitation from the terminal $1s$ level into a $b_2^*$ orbital corresponds to a transition from the $A_1$ ground state to $A_2$ and $B_2$ excited states. The former is dipole forbidden and the latter polarized in the $x$ direction. Thus we end up with the same result as in the unbroken symmetry treatment above.

Transitions from a terminal $1s$ orbital into $a_1^*$ or $b_2^*$ molecular orbitals yield broken symmetry configurations given by $a' \rightarrow a'$ transitions. Forming a linear combination from each pair of broken symmetry configurations in the $C_s$ point group result in two final states of $A_1$ and $B_2$ symmetry in the $C_{2v}$ point group. Thus for each of the transitions to an $a_1^*$ or $b_2^*$ molecular orbital there is a total of two final states. The energy separation between these two states will be extremely small and not resolvable. Therefore the transition will have its maximum when the light polarization vector is in the $z, y$ plane. This result is identical to that of the delocalized picture with unbroken symmetry.

However one must remember that this is just a study of possible transitions regarding symmetry considerations. The dependence of the intensity of a particular feature on the angle of the light polarization vector in the molecular plane for the transitions to $a_1^*$ or $b_2^*$ type orbitals cannot be predicted, either by using the broken or the unbroken model, and would require calculation. E.g. such a calculation for the terminal $O1s \rightarrow 7a_1 * (\sigma)$ transition in $O_3$ shows that the transition dipole moment is predicted at an angle close to the $\sigma$ bond between the terminal and central oxygen atoms [21], this is used in paper II. Furthermore, in the $SO_2$ case the picture is totaly different, here the dipole moment is parallel to either the $y$ ($B_2$ symmetry) or the $z$ ($A_1$ symmetry) axis, see paper III.

### 2.3.3 The Franck-Condon Principle

In addition to the symmetry properties for a transition also vibrational properties have to be taken into account. According to the Born-Oppenheimer approximation the nuclei can be considered fixed in space during an electronic transition. This means that all transitions must be vertical within the so called Franck-Condon region, defined by the ground state wave function (shaded in Fig. 2.4). The transition probability, reflected in the absorption efficiency (sketched in the left part of the figure), is proportional to the square of the overlap integral for the initial and final state vibrational wave functions for transitions to a bound state [processes (1) and (2) in Fig. 2.4]. If the internuclear distances are similar for the initial and final states, case (1), the overlap will be largest for the lowest vibrational transition ($v = 0 \rightarrow v' = 0$) and then declining. On the other hand, if the internuclear distances are displaced relative to each other, case (2), the overlap for the lowest vibrational transition is low and the maximum overlap occurs for some other vibrational transition. In this case for the $v = 0 \rightarrow v' = 3$ transition. Thus from electron spectroscopy or absorption spectroscopy information on the potential energy surface can be found. For a bound state the vibrational

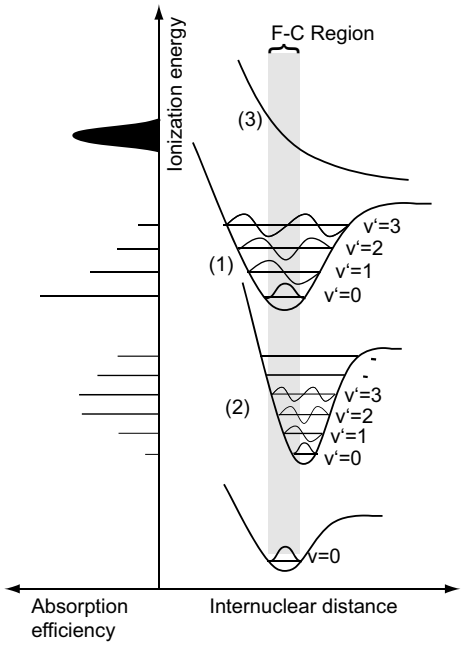


**Figure 2.4**: A sketch of the Franck-Condon principle: only transitions between states within the shaded area are possible. For transitions to bound states, case (1) and (2), the absorption efficiency is proportional to the square of the overlap integral of the vibrational wave functions.

spacing reflects the vibrational energy (both harmonic and anharmonic information) and the intensity distribution gives information on the internuclear distance. For transitions to repulsive states, case (3) in Fig. 2.4, the absorption spectrum exhibits no vibrational structure.

## 2.4 Relaxation after Photoabsorption

Core electron excitation or ionization creates a vacancy which for low Z material usually is filled by an electron from the valence orbitals and the excess energy is given to another valence electron which is emitted from the system. This process is commonly denoted as Auger decay and happens normally on a femtosecond (fs) time scale. A competing process is radiative decay, but for low Z material this is much less probable. In the energy domain of core electron excitation also autoionization after the initial Auger decay is common; thus the system ends up in multiply charged states which normally dissociate rapidly.

The terms dissociation or fragmentation will be used throughout this text to indicate breaking of a molecule into two or more ionic or neutral atomic or molecular fragments. In each dissociation the fragments are given kinetic energy, this will be refereed to as kinetic energy released (KER). Generally the KER can be attributed to the contribution from a lowering in the potential energy (see Fig. 2.5) or a repulsive energy originating from the Coulomb force between two charged fragments. The latter normally lead to higher KER.

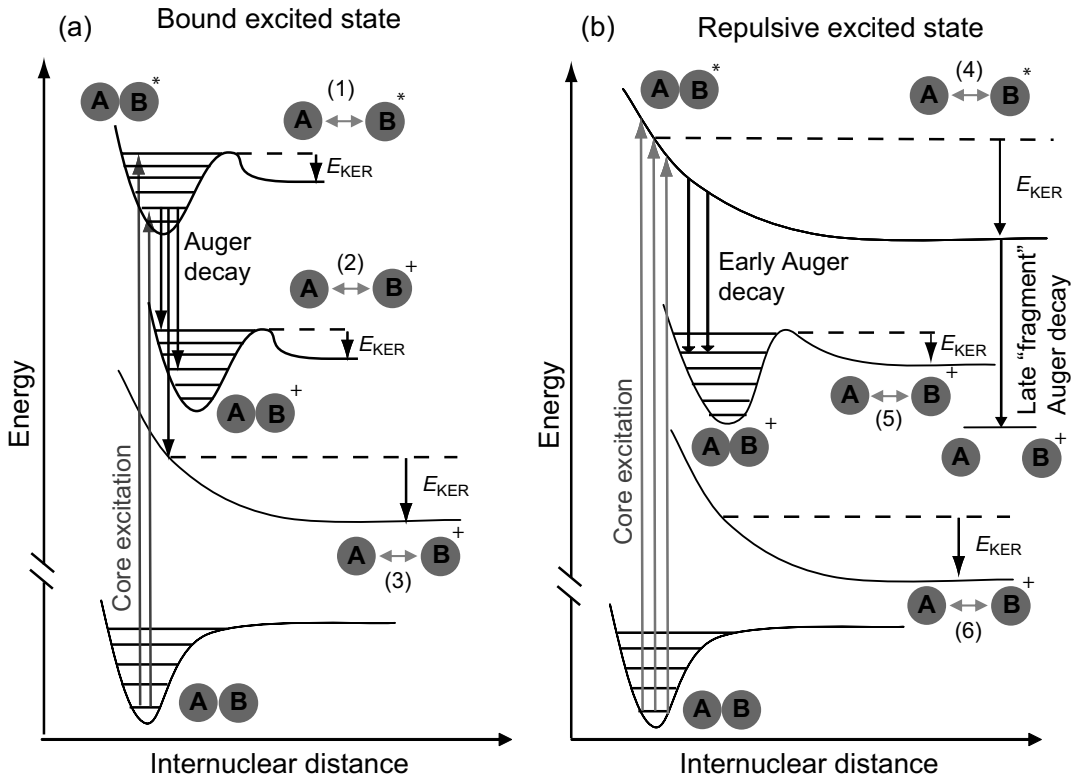


**Figure 2.5**: Some different dissociation processes possible after core excitation to a bound core excited state (a) or a repulsive core excited state (b). (1), (2) and (5) dissociation by tunnelling through the potential barrier in a high vibronic state. (3) and (4) dissociation in a repulsive state.

### 2.4.1 Dissociation

As an example we will have a look on dissociation after core excitation. The illustration in Fig. 2.5 is made for a diatomic molecule, AB, but can be extended to polyatomic molecules as well although the potential surface will be more complicated. I will discuss both the dissociation processes exciting to a bound or repulsive excited state.

In Fig. 2.5 (a) some possibilities for dissociation after a core excitation to a bound state are sketched. In case (1) the excitation results in a vibrationaly excited state from which dissociation can occur by tunnelling through the potential barrier. If present, this channel must be faster than the typical Auger life-time which is most unlikely after core-excitations. The process of tunnelling out from a bound state can also happen after the Auger decay (2), normally this type of intermediate state is expected to be ”long-lived” thus the molecule is believed to have time to vibrate (order of fs) and/or rotate (order ps) before dissociation. The pathway leading to the fastest dissociation occurs when the Auger decay populates a repulsive potential (3) [order of fs].

In the case of a repulsive excited state, Fig. 2.5 (b), a dissociation channel occurring before the Auger decay is opened (4). This process is called ultra fast dissociation [22, 23] and clearly happens faster than some femtoseconds. If the Auger decay anyway occurs before this ultra fast dissociation it can populate either a bound or repulsive state as shown in the figure, (5) and (6). And the dissociation process will be as described above.

This picture is highly schematic illuminating several classes of dissociation. E.g. the repulsive potential surfaces can have a small "well" somewhere for a certain geometry thus delaying the dissociation process. Surfaces with small "wells" are used to explain metastable ionic states, as found for e.g. $CO^{2+}$ [24] and $CO_2^{2+}$ [25].

In the above description only dissociation into singly ionized final states is depicted. This is not always the case, thus also double and multiple ionized states can be formed, as seen in the experimental results presented in the papers. There are mainly two different ways to produce these higher ionized states; direct double or higher ionization or autoionization of a molecular ion or fragment, depending on whether ultra fast dissociation is present or not. The time frame for the autoionization steps is normally in the same range as the initial Auger decay (fs).

**Energy Detuning**

By assuming only vertical transitions, inside the Franck-Condon region, an energy detuning can be performed. In case of a repulsive core excited state, e.g. Fig. 2.5 (b), both the "high" and "low" energy sides can be mapped. The studies of ultra fast dissociation are done in this way. By studying photo-electron spectra Auger decay from both molecular and "fragment" species are found. The kinetic energy of the Auger electrons from the molecular contribution varies with detuning photon energy whereas in the case of "fragment" Auger decay the electrons have a constant kinetic energy.

In ion spectroscopic measurements the effect of ultra fast dissociation is expected to be seen as different kinetic energy of the fragments depending directly on the detuning energy. Normally the ultra fast dissociative channel is weak and its signature is hard to separate from the signal of the other dissociation mechanisms producing the same fragments.

### 2.4.2 Alignment upon Photo-excitation

As described in section 2.3.2 a molecule absorbing linear polarized light will undergo an electronic transition from an initial state to some final state only when the molecule is specifically oriented with respect to the polarization direction of the incident light. The preservation of the alignment upon dissociation depends primarly on the time-scale. As discussed above the Auger life time is on the order of fs giving a lower time limit for the dissociation if the ultra fast dissociation is excluded. In case of preserved alignment an upper time-limit for dissociation is the rotational period which is on the order of picoseconds for small molecules. On the other hand, the time scale of bending motion is in the fs regime, thus it can be seen in the dissociation pattern [7] as geometry changes. The alignment of the molecules upon photo-excitation and its influence on the spectra is discussed more in Chap. 5.

If we exclude the ultra fast dissociation, the pathways we study after resonant excitation are Auger decays which populate either a bound or a repulsive potential energy surfaces. In the latter case the dissociation is very fast, thus both the induced alignment and the geometry of the core excited state should be preserved, case (a) in Fig. 2.6. On the other hand, by populating a potential energy surface containing a "well", vibrations and/or rotations can occur before the dissociation. The induced alignment would be lost if rotation has time to occur. But if "only" vibrational motion takes place the alignment is kept, although in the case of polyatomic molecules it will be "smeared out". This due to different bond angles at the moment of dissociation, case (b) and (d) in Fig. 2.6. The branch (c) in Fig. 2.6 will only

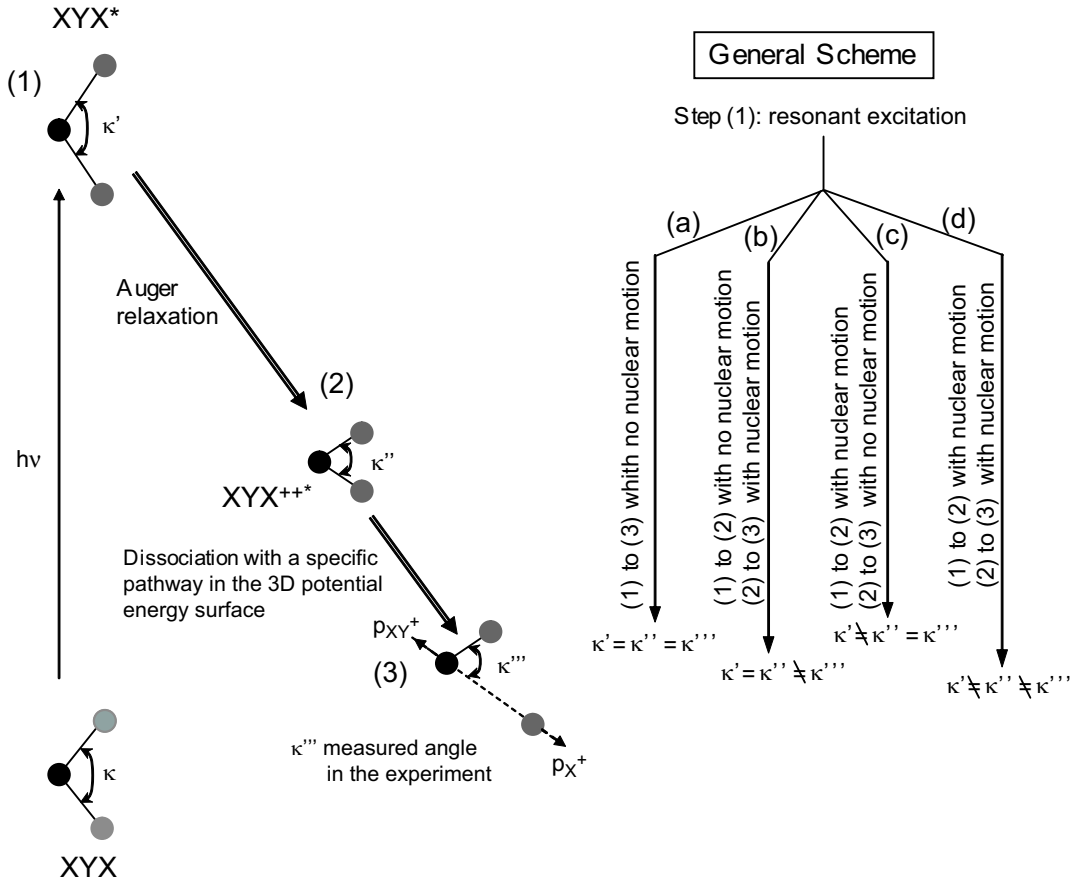


**Figure 2.6**: Some pathways of nuclear motion for a bent triatomic molecule after core excitation. For more information see the text.

occur if the Auger decay is slow enough for nuclear motion to take place. The dissociation of a specific core excited state does not always follow one route in the scheme, many different states are believed to contribute.

### Distribution in Space

An effect of the alignment is the anisotropic distribution in space of the ions formed. To describe this the anisotropy parameter, $\beta$, is used [26]. For linearly polarized light the angular distribution of photofragments can be expressed by:

$$d\sigma/d\Omega = \sigma_t/4\pi[1 + \beta P_2(\cos\vartheta)] \tag{2.12}$$

where $d\sigma$ is the differential absorption cross section, $d\Omega$ the solid angle unit, $\sigma_t$ is the total absorption cross section integrated over space, $\vartheta$ is the angle between the polarization vector and the dissociation direction and $P_2 = (3\cos^2\vartheta - 1)/2$ which is the second order Legendre polynomial. The $\beta$ parameter can range from +2 for a pure "parallel" transition (e.g. a $\Sigma \rightarrow \Sigma$ transition in a diatomic molecule) to -1 for a pure "perpendicular" transition (e.g. a $\Sigma \rightarrow \Pi$ transition in a diatomic molecule). "Parallel" and "perpendicular" represent the direction of dissociation in relation to the polarization vector. In the diatomic case an intermediate value

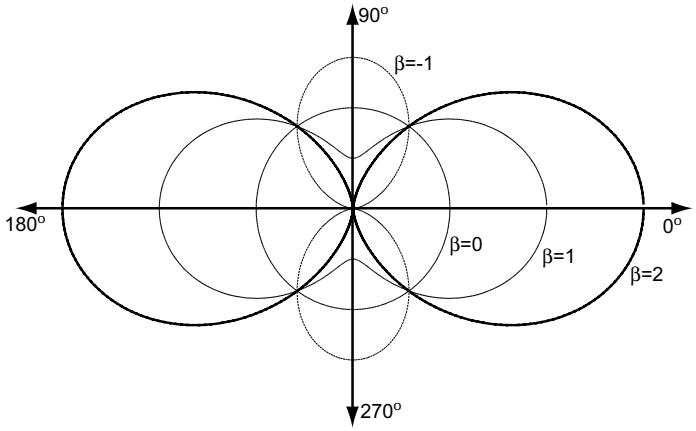


**Figure 2.7**: A sketch of angular distributions for different $\beta$ values. The angle used is $\vartheta$ in eq. 2.12. An interesting point is that when $\vartheta$ is $54.7°$ the angular distributions is the same for all $\beta$ values, this is useful for measurements independent of the angular distributions.

either indicates that both "parallel" and "perpendicular" transitions are being accessed or that the induced alignment is not preserved due to rotation.

For a polyatomic molecule an intermediate $\beta$-value indicates that the dissociation direction is not the same as the symmetry axis of the molecule and it could even indicate that the molecule has time to vibrate before dissociation. The connection between the $\beta$-value and the bond angle is not straight forward. But if the symmetry and thus the alignment of a core excited state is known it is possible to connect them. The $\beta$-value and the angle between the polarization vector and the broken bond, $\vartheta$ in the description above, is given by [27, 28]:

$$\beta = 3\cos^2\vartheta - 1. \tag{2.13}$$

Depending on the symmetry of the excited state $\vartheta$ will then be half the bond angle, or its complement angle.

A sketch of angular distributions for different $\beta$-values can be seen in Fig. 2.7, which also shows that a $\beta$ value of 0 corresponds to an isotropic distribution.

Chapter 3

# Rare-gas Clusters

Combining atoms or molecules into aggregates can be done. If these aggregates are intermediate in size (between the size of an atom and an infinite solid) they are called clusters. Thus the number of particles in a cluster is somewhere between a few (2-3) up to some thousands; the size of a cluster is thus on the nanometer scale. Clusters are interesting to study in order to follow the evolution of matter properties, from atomic/molecular size to infinite solid. A famous example of a cluster is the $C_{60}$-fullerene first formed by vaporizing graphite by laser irradiation. This stable cluster consisting of 60 carbon atoms structured as a polygon with 60 vertices and 32 faces, 12 of which are pentagonal and 20 hexagonal. The $C_{60}$ cluster, which results when a carbon atom is placed at each vertex of a truncated structure, has all valences satisfied by two single bonds and one double bond. Despite the highly stable geometry several studies show a characteristic fragmentation pattern where carbon dimers are evaporated.

Rare-gas closed-shell atoms (and also different molecules) can also be bonded together to form clusters. The force holding them together is the van der Waals attraction. The physical mechanism of the weak van der Waals force between closed-shell atoms is electric dipole interaction, arising from the quantum nature of electrons in the atoms. Condensation, or aggregation of a gas can be achieved through an adiabatic expansion of a supersonic jet, leading to cooling of the gas. Although the jet itself is cooled, substantial internal energy remains. They cool further by evaporation of atoms and after about $10^{-4}$s "stable" crystalline clusters are formed [29]. The amount of atoms in each cluster is normally decided by a so called "magic number", as in the case of the $C_{60}$ fullerene. The mechanism behind artificial production of snow in a snow-cannon is actually similar to the cluster source, which is descried in Sec. 3.2. But I will now start by a short introduction on relaxation of excited and/or ionized rare gas clusters.

## 3.1 Relaxation after Photoabsorption

A model describing the relaxation processes after mainly outer valence ionization, where single ionization is dominant, is presented by Haberland in [29]. In this model the electron leaves the cluster less than a femtosecond after photoabsorption. Hole hopping takes place in the unrelaxed cluster until the delocalized charge is localized to a dimer; this happens after about a picosecond. Dimer ions have dissociation energies of about 1 eV, so this amount of energy is "gained" when a dimer ion is formed and must be distributed within the cluster. This leads

to a temperature increase which will be followed by evaporation of neutral atoms in order to "cool" down the cluster again.

After inner-valence excitation or ionization the model needs to be modified [30], mainly due to relaxation processes leading to double ionization. After double/multiple ionization where the charges are localized to one atomic site in the cluster, the Coulomb forces tend to fission the clusters. Due to efficient charge transport mechanisms in competition with Coulomb forces, this fission results in the formation of singly charged fragments [30, 31]. The photon energy mainly determines the degree of ionization and no direct energy dependence is expected [30, 32]. For each ionization degree, the multiply charged species stabilize (within a $\mu$s time scale) when a critical size ($N_c$) is reached. Due to the weakly bound nature of van-der-Waals clusters, the critical size ($N_c$) is always high ($> 50$ atoms). Thus, cluster fission varies gradually with the degree of ionization and the cluster size. In Fig. 3.1 (a) an illustration of the sequence of possible processes is shown.

The absorption process is photon energy dependent as described in Sec. 2.2, but no resonant alignment effects are expected due to a large variety in orientation, geometry and size of the produced clusters. The hole produced by photo-absorption is primarily stabilized by either electronic or radiative relaxation.

Direct photo-ionization below the $2p$ threshold in the argon cluster clearly produces a localized ionic site. Single, double and even triple ionization have significant probabilities, and multiply-ionization quickly leads to charge migration from the initial ionization site, generally before the evaporation of neutral atoms [32]. Neighboring charged units (dimer or atoms) exert a repulsive force which can lead to 'Coulomb explosion' where fragments gain significant kinetic energy, especially in the case of highly charged species [30, 33]. However, this process is not confirmed specifically for clusters, and studies of doubly-charged dimers reveal a kinetic-energy release which exceeds the level expected for Coulomb repulsion [34]. Large clusters naturally have more complex dissociation behavior where evaporation of neutral atoms, and stability based on fragment or cluster size play a role. These processes are significant in determining important fragmentation mechanisms in clusters. An additional complication arises in multiple electronic decay cascades. Inelastic scattering is well known in condensed matter; diffraction of photoelectrons and energy loss processes are apparent in a variety of studies. Clearly such phenomena are of importance in clusters, and are compounded by multiple ionization where several electrons are produced. Scattering can lead to fragmentation, electronic excitation or ionization, and is highly dependent on the electron kinetic energy.

For resonant electronic relaxation in rare-gas clusters we expect an atom in a two-hole one-particle configuration to be formed after resonant Auger decay within the cluster. If this state is below the vertical double ionization potential no doubly charged fragments or multiple coincidence events would be found in the ion spectra. In paper VI we find strong evidence to the contrary. A probable explanation for this is a lower adiabatic double ionization potential reachable by nuclear rearrangements and curve crossings as illustrated in Fig. 3.1 (b).

## 3.2 Cluster Source

The cluster experiments were carried out using a cluster source based on adiabatic gas expansion [35]. The expansion is performed from a high pressure stagnation chamber into vacuum through a small nozzle. Different nozzle shapes (conical, flat) and diameters were

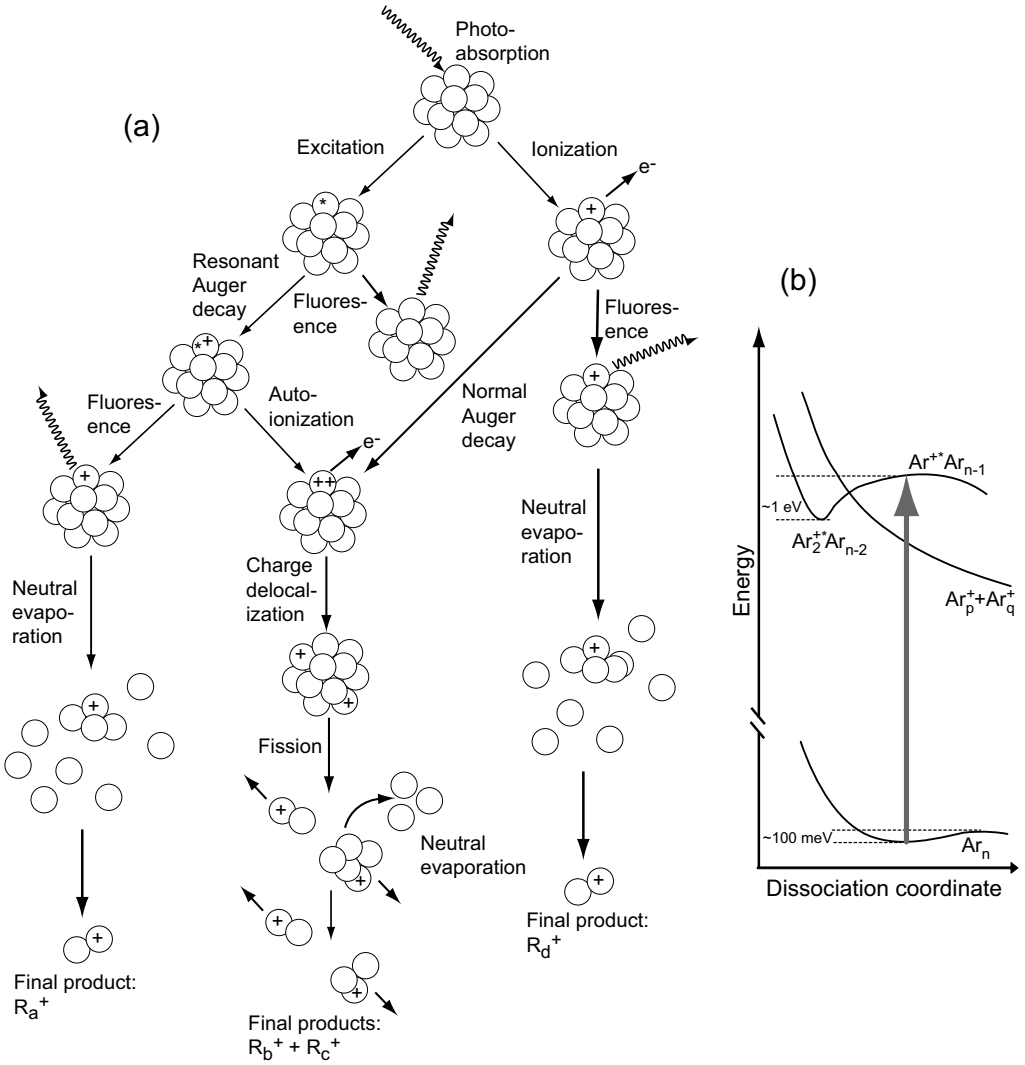


**Figure 3.1**: (a) A schematic illustration of the processes occurring after inner valence excitation or ionization. (b) Lowering of the double ionization potential by nuclear rearrangement and curve crossing, as seen after resonant Auger relaxation of the $2p_{3/2}^{-1}4s^1$ state in small argon clusters.

used to produce different cluster sizes. The nozzle was mounted on an $xyz$ manipulator, to be able to control the position of the beam. The gas beam formed in the expansion chamber of the cluster source was skimmed with a conical copper skimmer, to get rid of most of the uncondensed gas, before entering the beam-line ionization chamber. A schematic picture of the cluster source can be found in Fig. 3.2.

The expansion creates clusters with a distribution of sizes around some mean value, $< N >$. By varying the expansion pressure and temperature as well as the shape of the nozzle, the mean size of the clusters created can be controlled. The nozzle used can be cooled in several ways; a cooling system based on Peltier elements allows cooling down to $-40°$C, and in combination with liquid nitrogen cooling nozzle temperatures ranging from $-80°$C to

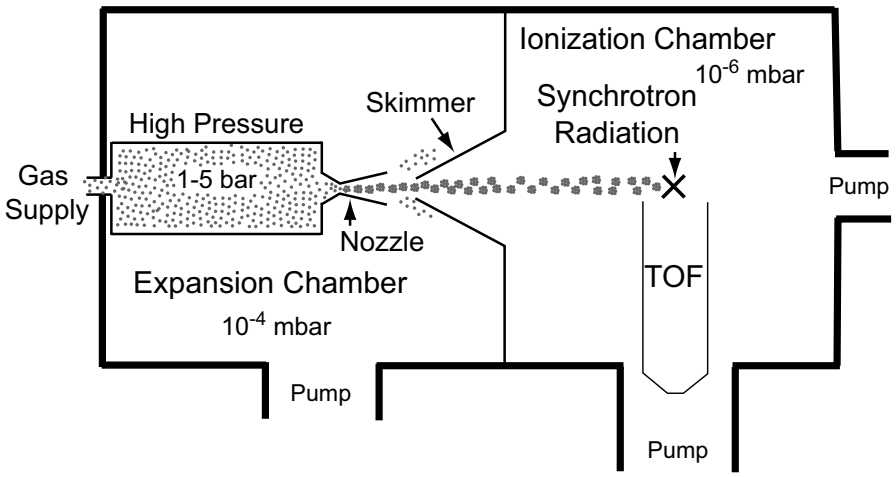


**Figure 3.2**: Schematic picture of the cluster source.

$-175°$C can be reached. The average size $< N >$ of the clusters can be determined from the expansion conditions using the scaling parameter $\Gamma^*$ formalism [36]. The distribution of sizes around this average can roughly be approximated by a Gaussian with a full width at half-maximum of $N/2$. The source successfully produces clusters in a wide size range; argon clusters are for example produced with $< N >$ ranging from a few atoms up to $50\,000$ atoms.

Chapter 4

# The Spectrometer

This chapter is devoted to the setup and characteristics of the time-of-flight mass spectrometer used for the photofragmentation measurements of core-excited molecules and clusters presented in this thesis. The main idea is to via electric fields collect the electrons and ions formed in the photofragmentation process. The electrons are used as a start signal and then the ions formed are measured in coincidence by recording there flight times. The design is a two-field Wiley-McLaren [37] type time-of-flight (TOF) ion mass spectrometer, to ensure that ions with the same mass, charge and momentum will get the same flight times independent of the formation point in the interaction region of the molecular beam and the photons. The main parts of the spectrometer are the extraction and the acceleration regions, a drift tube and two Multi Channel Plate (MCP) detectors (used in a chevron set-up). A sketch of the spectrometer is given in Fig. 4.1. The spectrometer has been optimized geometry and electric field strength wise in order to reduce discrimination against electron and ion momenta. We also have the ability to mount the spectrometer both parallel and perpendicular relative the polarization vector of the excitation photon beam. The acquisition setup is chosen such as it allows a multihit capability of about 4 ns and binning of 1 ns. Hereby, coincident measurements on molecules containing two or more atoms of equal mass and detailed analysis of the peak shapes due to small differences in the kinetic energy of the ions of the same kind can be performed. The characteristics of the spectrometer and the data collection systems will be discussed in the following sections.

## 4.1 Flight Time Calculations

The flight time for an ionic fragment with charge, $q$, mass, $m$, and initial kinetic energy along the spectrometer axis, $U_0$, in a two field TOF-spectrometer (Fig. 4.1) can be divided into three parts according to the three different regions in the spectrometer (extraction-,

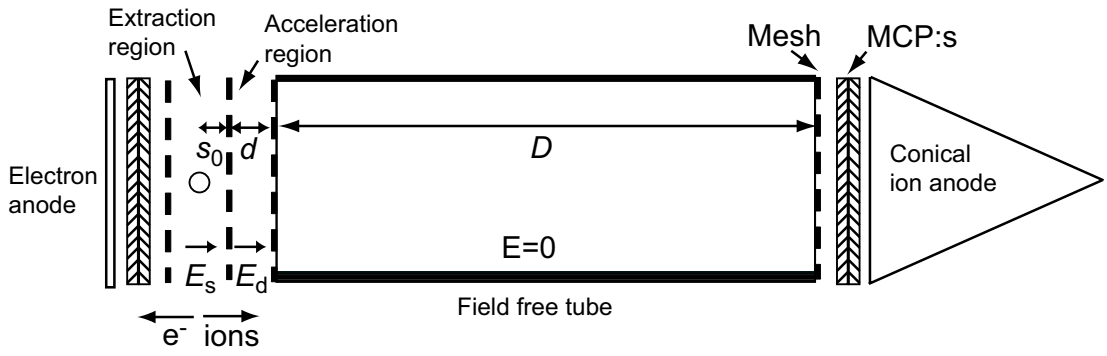


**Figure 4.1**: A schematic drawing of the coincidence spectrometer. The ions and electrons are formed in the source region, indicated by the circle in the extraction region. The size of the source region is defined by the gas and synchrotron radiation beams. The distances $s_0$, $d$ and $D$ in our spectrometer are $6/2 = 3$ mm, 5mm and 121 mm. Typical fields used are some hundreds to thousands of V/cm.

acceleration- and drift-regions, $T_\mathrm{s}$, $T_\mathrm{d}$ and $T_\mathrm{D}$ respectively) and can be expressed as [37, 38]:

$$T_\mathrm{s} = \frac{\sqrt{2m}}{qE_\mathrm{s}}(\sqrt{U_0 + qsE_\mathrm{s}} \pm \sqrt{U_0}) \tag{4.1a}$$

$$T_\mathrm{d} = \frac{\sqrt{2m}}{qE_\mathrm{d}}(\sqrt{U} - \sqrt{U_0 + qsE_\mathrm{s}}) \tag{4.1b}$$

$$T_\mathrm{D} = \sqrt{2m}\frac{D}{2\sqrt{U}} \tag{4.1c}$$

where $s$ is the length of the ion flight path in the extraction region, $d$ is the length of the acceleration region and $D$ is the length of the drift tube whereas $E_\mathrm{s}$ and $E_\mathrm{d}$ are the electric fields in the extraction and acceleration regions respectively. $U = U_0 + qsE_\mathrm{s} + qdE_\mathrm{d}$ is the total kinetic energy of an ion in the field free drift tube. $U$ is independent of $m$ so all ions with the same charge will have the same kinetic energy when hitting the detector. The total flight time will thus be:

$$T = T_\mathrm{s} + T_\mathrm{d} + T_\mathrm{D} \tag{4.2}$$

### 4.1.1 Space Focus

According to equations (4.1) both $s$ and $U_0$ will affect $T$. Thus ions with the same mass to charge ratio can have different flight times depending on where and with which kinetic energy they are formed. The result will be peaks in the TOF spectrum whose shapes are influenced by these parameters together with field inhomogeneities.

We are interested in measuring the energy distribution of the ions thus we want to minimize the spatial dependence on the peak shapes. This can be done by applying the so called space focusing condition [37]. The condition can be formulated: Identical ions formed at slightly different distances from the center of the source region shall have the same flight time.

Since an ion created closer to the detector acquires less energy than an ion created further away from the detector, the former eventually overtakes the last resulting in different flight times. This time difference will cancel if it is possible to find a combination of the parameters

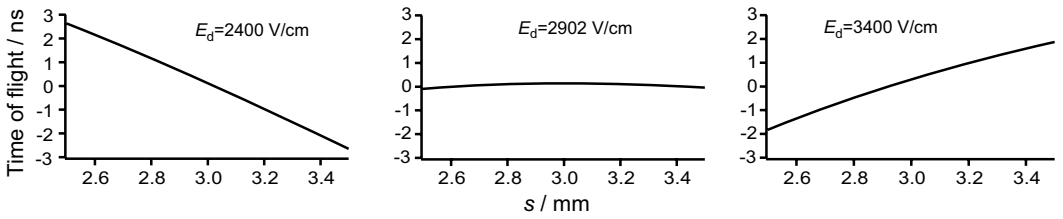


**Figure 4.2**: Flight-time distributions as a function of the distance travelled in the extraction region for an ion of mass 16 amu and charge $+1e$ for some different acceleration fields. The extraction field was fixed to 666.66 V/cm and the length of the acceleration region and drift tube was 5 mm and 121 mm respectively, just as they are in the spectrometer we used. The source region in our case is approximately 0.4 mm wide and the middle of the source is located with an $s$ of 3 mm. In the middle plot the space focusing condition is fulfilled.

determining the flight time which minimizes the flight-time difference between the two ions. To perform the analysis we will set $U_0 = 0$ and $s = s_0$, where $s_0$ is the distance from the center of the extraction region to the beginning of the acceleration region. Then the total flight time can be expressed as:

$$T(U_0 = 0, s_0) = \sqrt{\frac{m}{q}\frac{q}{2U_t}}\left[2\sqrt{k_0}s_0 + \frac{2\sqrt{k_0}}{\sqrt{k_0}+1}d + D\right], \tag{4.3}$$

where $U_t$ is

$$U_t = qs_0E_\mathrm{s} + qdE_\mathrm{d} \tag{4.4}$$

and $k_0$ is defined as

$$k_0 = \frac{s_0E_\mathrm{s} + dE_\mathrm{d}}{s_0E_\mathrm{s}}. \tag{4.5}$$

Two ions formed at the positions $s_\mathrm{max} = s_0 + 0.5\Delta s$ and $s_\mathrm{min} = s_0 + 0.5\Delta s$ , where $\Delta s$ is the diameter of the source region defined by the photon beam and the gas jet, will then have very similar flight times when $(dT/ds)_{U_0=0,s_0} = 0$. From this condition we can find that the optimal length of the drift tube for given sizes of the extraction and acceleration regions as well as the magnitude of the electric fields in these regions can be given by [37]:

$$D = 2s_\mathrm{o}\sqrt[3]{k_0}\left[1 - \frac{1}{k_0 + \sqrt{k_0}}\frac{d}{s_\mathrm{o}}\right]. \tag{4.6}$$

In practice, for a two-field system, the geometrical dimensions $s$, $d$ and $D$ can be fixed and the ratio between $E_\mathrm{s}$ and $E_\mathrm{d}$ is determined to set the space focusing condition. For our geometry the ratio is: $E_\mathrm{d}/E_\mathrm{s} = 4.354$. To illustrate the space focusing condition a calculation using equation (4.3) is presented in Fig. 4.2. Here we used the geometry of our spectrometer, fixed the extraction region field to 666.66 V/cm and used ions of mass 16 amu and charge $+1e$. In the figure it is clear that the ion flight time is independent of its initial position in the extraction region if the space focusing condition is satisfied (middle plot in Fig. 4.2).

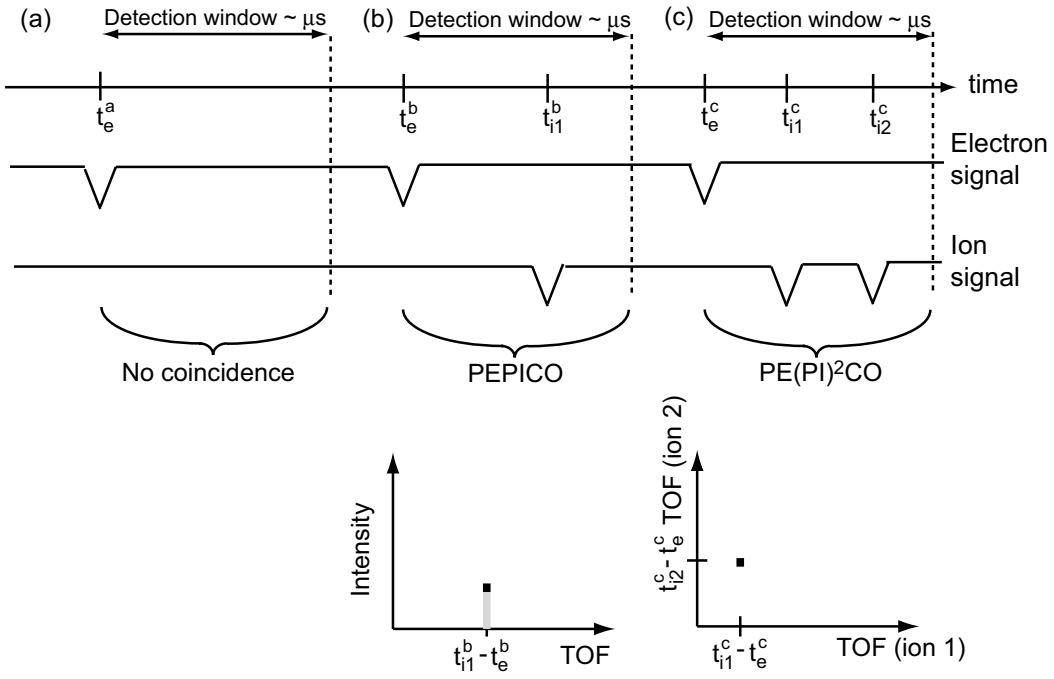


**Figure 4.3**: A schematic on how the ion time of flights are measured. The electron signal is used as a start signal for the ion detection window. In (a) no ion is detected during the preset ion detection window whereas in (b) and (c) one (PEPICO) and two ions (PE(PI)$^2$CO) are detected. At the bottom of the figure an illustration of the data presentation is shown.

## 4.2 Data Acquisition

All charged particles formed after an ionization or fragmentation process are accelerated by the static electric fields which accelerates the ions according to their charge and mass as seen in the former section. After travelling through the field-free region the particles are detected, and the time interval from their creation is measured. To be able to know when the ionization took place the energy-unresolved (fast flying) electron is used as a start signal. The flight time for the different ions are measured by taking the difference between the electron and the ion signals, therefore the method is called PhotoElectron-PhotoIon$^{\mathrm{X}}$-COincidence (PE(PI)$^{\mathrm{X}}$CO) [1, 2, 3, 39] where the X indicate the number of ions detected.

In Fig. 4.3 a schematic of some different scenarios are shown. In (a) there is no ion signal during the ion detection window (the ion detection window is preset in the electronics), so this event is discarded. Case (b) shows the example when one ion is detected within the detection window and case (c) shows when two ions is detected. Thus we measure all the ions after an ionization event and the data are stored as an array

$$(t_1, t_2, ...t_{\mathrm{n}}), \tag{4.7}$$

where $t_{\mathrm{i}}$ is the flight time for the i:th ion hitting the detector. This can later be compacted by storing as a histogram. The events where only one ion is detected after the starting electron signal, PEPICO, are sorted into a histogram consisting of the amount of events at each flight time whereas the events where two ions are detected after a start, PE(PI)$^2$CO, are sorted into

**Table 4.1**: A sample of stored data. The two first columns show a sequence of PEPICO data, the TOF column contains the flight time in ns and the counts column contains the number of ions with this flight time. The PE(PI)$^2$CO data are stored as shown in the three right columns, the columns T1 and T2 are the flight times for the first and second ion respectively whereas the counts column contains the number of ion-pairs with this time pair.

| TOF | counts | T1 | T2 | counts |
|---|---|---|---|---|
| 75 | 8496 | 75 | 822 | 35 |
| 76 | 20015 | 75 | 823 | 63 |
| 77 | 42223 | 75 | 824 | 89 |
| 78 | 76769 | 75 | 825 | 151 |
| 79 | 126041 | 75 | 826 | 193 |
| 80 | 175183 | 75 | 827 | 229 |
| 81 | 211822 | 75 | 828 | 228 |
| 82 | 239799 | 75 | 829 | 222 |
| 83 | 262687 | 75 | 830 | 180 |
| 84 | 275367 | 75 | 831 | 164 |
| 85 | 262836 | 75 | 832 | 124 |
| 86 | 234669 | 75 | 833 | 84 |
| 87 | 201437 | 75 | 834 | 49 |
| 88 | 163818 | 75 | 835 | 22 |
| 89 | 121800 | 75 | 836 | 10 |
| 90 | 74734 | 75 | 837 | 10 |
| 91 | 40760 | 75 | 838 | 3 |
| 92 | 19598 | 75 | 839 | 3 |
| 93 | 8322 | 75 | 840 | 3 |

a histogram consisting of the amount of counts at each time pair and so on for higher degree of coincidences. Examples of such histogram matrices can be found in Table 4.1. The two first columns show a sequence of PEPICO data and last three columns show a sequence of PE(PI)$^2$CO data. These are then displayed as either a two dimensional intensity vs. time spectrum (PEPICO) or time vs. time contour plot (PE(PI)$^2$CO) [1]. An illustration of this can be seen in the bottom of Fig. 4.3 for the different cases. For all data presentation in the thesis we used 1ns binning in order to have high resolution on the kinetic energy of the ions.

### 4.2.1 Detection Efficiency

In the presentation above we assumed that all electrons and ions formed also are recorded with the spectrometer. Lets consider the case in Fig. 4.3 (c), if one of the ions formed is not detected by the spectrometer we would not get a signal and that event would be regarded as a PEPICO event instead. Thus the recorded PEPICO event is an aborted PE(PI)$^2$CO event. This effect (detection efficiency) mainly depend on three factors;

- Geometry and field strength in the spectrometer factor.
- The transmittance of the meshes.
- Probability that a signal is generated at the detector.

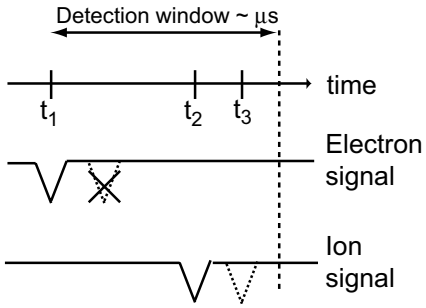


**Figure 4.4**: An illustration of a false coincidence. Unwanted signals are shown with dotted lines. The "false" start in the electron signal is disregarded but the "false" stop in the ion signal is recorded resulting in a false PE(PI)$^2$CO event.

Of these three factors the first one can almost be neglected through clever spectrometer design. The particles with highest kinetic energy might be lost. The maximum kinetic energy of the electrons and ions that can be collected can be simulated by using e.g. the ion optics simulation program SimIon 3D 7.0 [40]. For our spectrometer, using an extraction field of 666.6 V/cm (and keeping the space focus criteria) all electrons up to 450 eV and ions up to 25 eV are collected without any angular discrimination. This was checked by performing measurements with the spectrometer both parallel and perpendicular to the electric field vector and comparing the number of ions and electrons collected. The total normalized signals were equal, confirming the result of the simulation. Thus this factor can normally be neglected in our spectrometer.

Considering the two other factors: The meshes we use have a transmission of about 80%. Because the ions encounter three meshes, about 50% of them will be transmitted to the detector. The transmission for electrons will be 80% because they encounter only one mesh on the way to the detector. The probability to generate a signal when the particle is hitting the detector depends on the type of detector used. MCP detectors have detection efficiencies of $\sim 40\%$ and $\sim 60\%$ for ions and electrons of some keV kinetic energy [41]. Thus considering the transmittance of the meshes the total ion detection efficiency can be estimated to $\sim 20\%$ and the total electron detection efficiency is estimated to $\sim 50\%$. But for the electrons it is sufficient to detect only one out of many electrons in order to start the measurement so in practice the detection efficiency for the start signal is higher for events where multiple ionization has taken place. E.g. the efficiency to detect at least one electron out of two is $\sim 75\%$.

### 4.2.2 False Coincidences

New dissociation events are unwanted during a detection window. An example is given in Fig. 4.4 where a false coincidence event is indicated by the dotted signals. During the ion detection window new start signals are disregarded, but the optimal condition for excluding events from other fragmentations is to reduce the frequency of measured events. This can be expressed as:

$$e^-_{\text{start}}(\text{Hz}) \cdot \text{detection}_{\text{window}}(\text{s}) << 1. \tag{4.8}$$

E.g. if the ion detection window is a $\mu$s the frequency of start signals shall be less than 10 kHz. This can be controlled by adjusting the intensity of the light and the gas pressure in the chamber.

## 4.3 Detector System and Electronics

### 4.3.1 Detector

The previous discussion has outlined several important detector properties for these measurements. These are:

- detect charged particles,
- large area,
- pulse widths ($< 1$ ns),
- good detection efficiency.

The Multi Channel Plate (MCP) detector used in our set-up is thus a good choice. It is good for detecting charged particles of varying masses. It can be produced with a large active area and the pulse widths are less than 1 ns and it has a fairly high detection efficiency. One more good property is that the operating voltages are well adapted for our system.

We used MCP:s from Burle [41] with a effective diameter of 40 mm. They were set up two and two in a chevron configuration to increase the amplification of the signal. The gain for this kind of set-up is about $10^7$ if a voltage difference of 1700-1800 V is kept over the two plates [41].

### 4.3.2 Data Storage System and Electronics

Amplification of the fast MCP signal is performed by Ortec 9306 preamplifiers [42] with a sampling rate of 1 GHz. To filter the true pulses from the background noise a leading edge discriminator (Phillips scientific Model 704 [43]) was used. The discriminator has a pulse-pair resolution of 3.3 ns [43]. A sketch of the pulse scheme is presented in Fig. 4.5. After the discriminators the signal is fed into a Time to Digital Converter (TDC), see Fig. 4.6. The

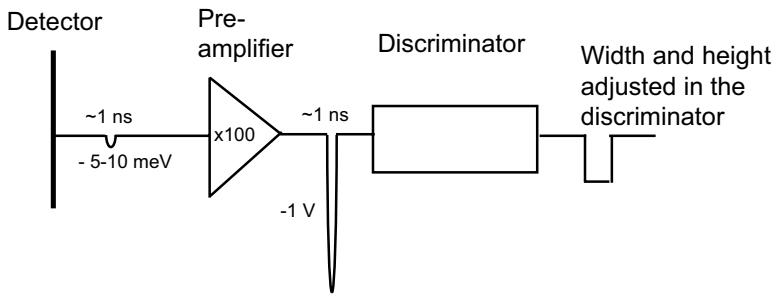


**Figure 4.5**: A scheme of the pulse shapes after the different component in the data collecting electronics.

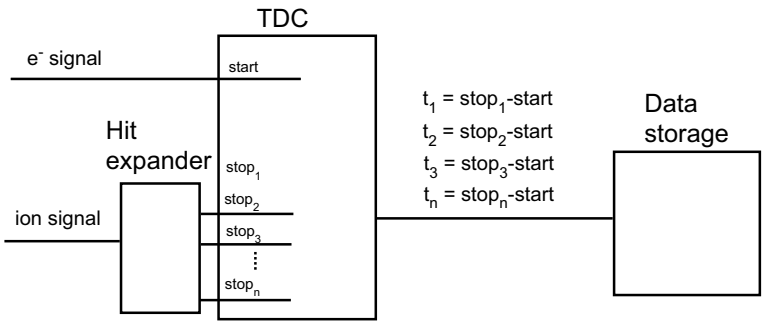


**Figure 4.6**: Illustration on how the Time to Digital Converter (TDC) works.

TDC is used to digitalize the TOF for the ionic fragments before the information is stored on a computer hard drive.

The system mainly used to process and store the data is built around a computer TDC-card, FAST P7886S, manufactured by Fast ComTec [44] with a multi-hit time resolution of 1 ns and a dead-time of 1 ns. The FAST card is installed in a Microsoft® Windows® based PC. The data collection software is developed by F. Burmeister *et al.* [45] using the data analyzing software Igor Pro [46].

Chapter 5

# Data Analysis of Electron Ion/Ions Coincidence Measurements

This chapter is devoted to descriptions of the methods used in the data analysis. I begin with a short introduction to some general aspects of time-of-flight spectroscopy of photofragments produced after core excitation, before going deeper into the models used to understand the spectra.

The time of flight (TOF), $t_{\mathrm{i}}$, for a particular ion, under the space focusing conditions discussed in sec. 4.1.1, can also be expressed [1]:

$$t_{\mathrm{i}} = t_{\mathrm{i}}^{0} + a\mathbf{p}_{\mathrm{i}} \cos\eta_{\mathrm{i}} \tag{5.1a}$$

$$t_{\mathrm{i}}^{0} = c + d\sqrt{\frac{m}{q}}, \tag{5.1b}$$

where $a$ is a constant depending on the fields and the geometry of the spectrometer, $\mathbf{p}_{\mathrm{i}}$ is the initial momentum of the fragment, $\eta_{\mathrm{i}}$ is the angle between the initial momentum and the spectrometer axis and $t_{\mathrm{i}}^{0}$ is the average TOF for an ion with mass, $m$, and charge, $q$, where $c$ and $d$ are parameters depending on the specific experimental set-up. Hence $t_{\mathrm{i}}$ provides information on both the mass-charge ratio and on the momentum of the ions. The mass-charge ratio can be found by the position of the peaks whereas the width gives information on the momentum and thus the kinetic energy of the ions. In addition the shape of the peaks reflects the alignment of the molecules upon an electronic transition.

In order to investigate the effect of fragment ion momentum on the flight time, it is convenient to consider two ions formed at the same position with the same kinetic energy but directed opposite to each other along the spectrometer axis. The ion moving away from the detector decelerates, due to the field in the extraction region, until it stops and then it is accelerated towards the detector. When it reaches the position where it was formed it has its original kinetic energy again but now in the direction towards the detector, just as the ion initially going toward the detector. This means that from this point the motion of the ion originally moving away from the detector is the same as for the one moving towards the detector and thus the flight time difference is due to the "turn around" time. This time difference, $\Delta T_{\text{turn around}}$, is given from eqn (4.1) to be:

$$\Delta T_{\text{turn around}} = \frac{2\sqrt{2mU_0}}{qE_{\mathrm{s}}} \tag{5.2}$$

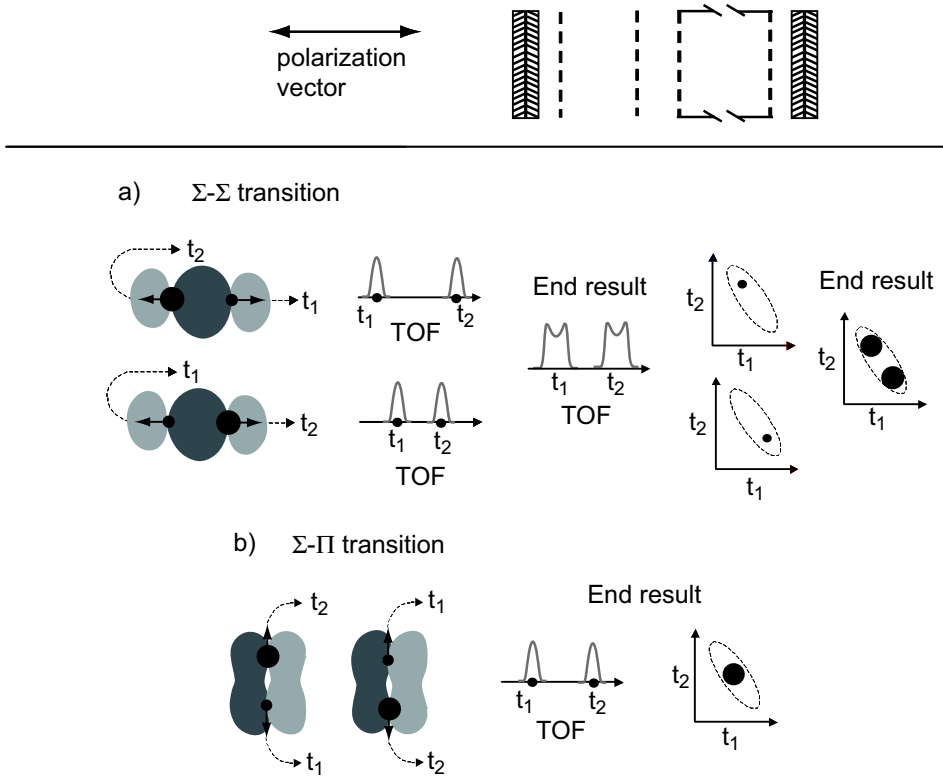


**Figure 5.1**: A schematic illustration of the influence on the flight time for different molecular alignments. The figure shows alignment after a $\Sigma \rightarrow \Sigma$ excitation (a) and a $\Sigma \rightarrow \Pi$ excitation (b) in a diatomic molecule e.g. CO. The spectrometer is mounted parallel to the polarization vector.

where $U_0$ is the kinetic energy of the ion and $E_s$ is the strength of the electric field in the extraction region. By applying different extraction fields, and adapting the accelerating field in order to satisfy the space focusing criteria, the flight time difference due to kinetic energy can be changed. Lower fields give higher flight time differences, at the cost of angular discrimination of high kinetic energy electrons and ions. The ”turn around” time can also be expressed as $a\mathbf{p}_i \cos\eta_i$ from eqn 5.1.

The effect of alignment is illustrated in Fig. 5.1. In (a) the situation for a $\Sigma \rightarrow \Sigma$ transition and in (b) the situation for a $\Sigma \rightarrow \Pi$ transition is shown. In Fig. 5.1 (a) the molecular axis is oriented parallel to the polarization vector and thus dissociation is parallel to the spectrometer axis. Here the two possible orientations of the molecule give different flight times for the light and heavy fragments ($t_1$ and $t_2$, respectively). In the upper orientation the light fragment will get a ”short” flight time and the heavy a ”long”. The opposite behavior is found below. The result seen in the TOF spectrum is a double peaked shape. Also the influence on a $t_2$ vs $t_1$ plot is shown. Here the two orientations contribute differently to the contour plot resulting in the intensity distribution seen in the figure. For the $\Sigma \rightarrow \Pi$ transition, Fig. 5.1 (b), the molecular axis is oriented perpendicular to the polarization vector and thus the dissociation is perpendicular to the spectrometer resulting in two possible orientations with the same flight times. The TOF spectrum and the $t_2$ vs $t_1$ plot will have a single peak.

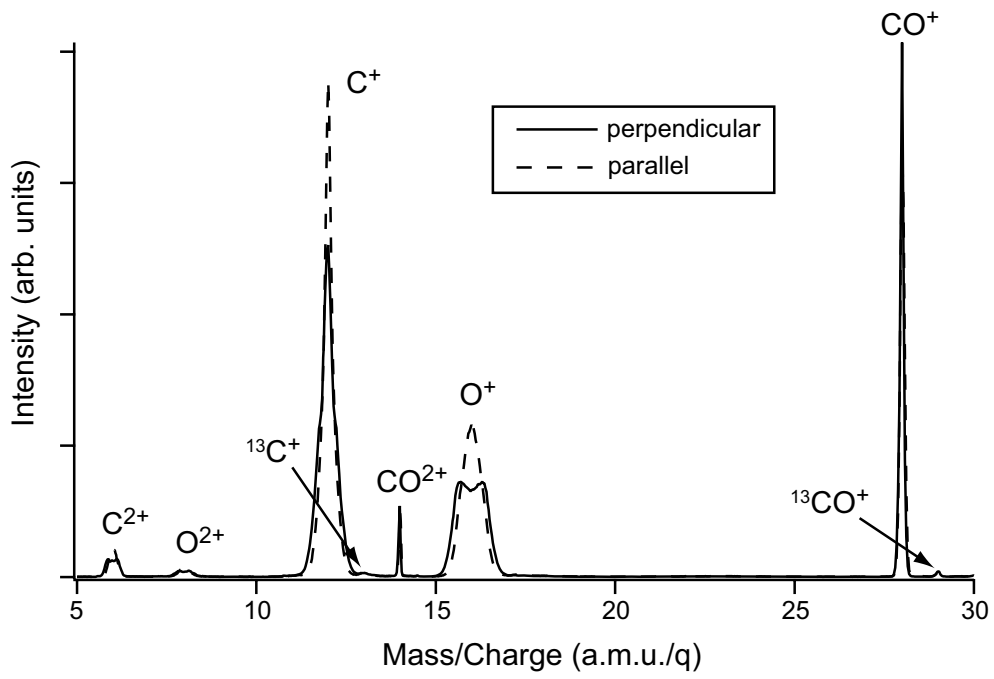


**Figure 5.2**: Mass-spectra collected after the C $1s \rightarrow \pi^*$ transition in CO, at $\sim$ 288 eV. The measurements are performed with the spectrometer parallel (dashed line) and perpendicular (solid line) to the radiation polarization vector.

The time frame for dissociation after resonant excitation can be found by analyzing the peak shapes. If alignment is confirmed, the anisotropy is preserved and thus the dissociation must at least be faster than the rotation. If nuclear motion has taken place the anisotropy reflects the mean value of the molecular geometry.

## 5.1 Mass Spectra

In Fig. 5.2 the mass spectrum (time-of-flight) for CO collected after the C $1s \rightarrow \pi^*$ transition is shown. The measurements are performed with the spectrometer both parallel and perpendicular to the light polarization vector. We use this spectrum to highlight some aspects of the data analysis.

First of all the time scale is converted into the mass over charge ratio via eqn (5.1b). The intensity distribution varies between the different peaks, thus the relative branching ratios can be deduced. Note that the integrated intensity of each peak in the parallel and perpendicular spectra is the same. Thus the collecting efficiency is the same for both the parallel and perpendicular measurements.

Turning to the widths of the peaks, the unfragmented $CO^+$ and $CO^{2+}$ peaks shows equal and narrow widths, as expected. On the other hand, the peaks originating from the fragments $O^+$, $C^+$, $O^{2+}$ and $C^{2+}$ have much larger widths, thus the fragments have relatively high momentum from the dissociation process. Here peak shapes differ with angle of the spectrometer. Thus the alignment of the molecules at the moment of the dissociation is clearly seen in the spectra. The C $1s \rightarrow \pi^*$ transition is expected to be aligned perpendicular

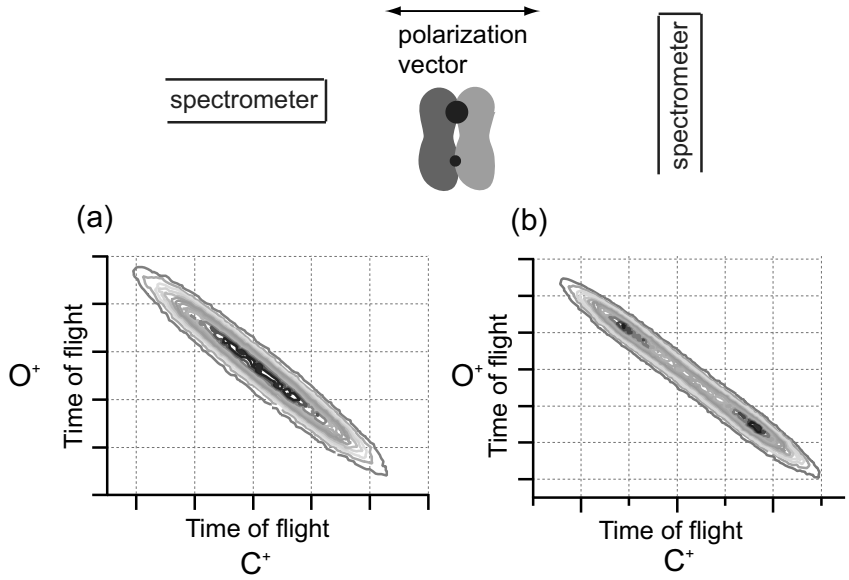


**Figure 5.3**: PE(PI)$^2$CO contour plots of the two-body channel $C^+$+$O^+$ after the C $1s \rightarrow 2\pi^*$ ($\sim$ 288 eV) transition in CO. In (a) the spectrometer is mounted parallel to the light polarization vector and in (b) it is perpendicular.

to the light polarization vector and thus an anisotropic distribution perpendicular to the polarization vector ($\beta$=-1). We expect that single peaked structures are seen in the case of polarization vector and spectrometer axis parallel and double peaked structures are seen in the perpendicular case.

## 5.2 Ion-coincidence Spectra

Lets consider processes where at least two ions originating from the same dissociation process are measured in coincidence with each other. In Fig 5.3 PE(PI)$^2$CO contour plots of the two-body channel $C^+$+$O^+$, measured after the C $1s \rightarrow 2\pi^*$ ($\sim$ 288 eV) transition in CO, are shown. The contour patterns clearly indicate perpendicular alignment of molecules to the light polarization vector. In (a) the spectrometer is mounted parallel to the light polarization vector and thus a single peaked structure in the PE(PI)$^2$CO plot is found. If instead the spectrometer is placed perpendicular to the light polarization vector, as in (b), the distribution in the time of flights as described above will result in a doubly peaked structure.

Until now we have only discussed diatomic molecules. If polyatomic molecules are considered the picture is complicated by the different dissociation pathways available together with the influence of bond and torsion angles on the alignment picture. Thus the anisotropic distribution is no longer only along or perpendicular to the radiation polarization axis. In order to describe the molecular orientation at the different core excitations we have chosen to use the bond angle and the type of symmetry instead of the anisotropy parameter $\beta$, but in case of a single bond break they can be connected through eqn (2.13) as described in Sec. 2.4.2.

In the following sections models describing the induced alignment, based on the symme-

try of the excitation, together with dissociation mechanisms for two and three-body dissociations are presented. In the case of two-body processes the data also give information on the bond angle and the kinetic energy released in the process. For the three-body processes a model giving the type of dissociation mechanism (sequential or concerted) as well as the momentum of the undetected fragment is presented.

### 5.2.1 Two-body Processes

Considering dissociations including exactly two fragments arising from the same dissociation event the momentum is conserved

$$\mathbf{p}_1 + \mathbf{p}_2 \approx 0 \tag{5.3a}$$

$$\mathbf{p}_1 - \mathbf{p}_2 \approx \mathbf{p} \tag{5.3b}$$

where $\mathbf{p}$ is the total momentum in the dissociation. Then the flight times, $t_1$ and $t_2$, for the two fragments will be:

$$t_1 = t_1^0 + a\mathbf{p}_1 \cos\eta \tag{5.4a}$$

$$t_2 = t_2^0 + a\mathbf{p}_2 \cos\eta. \tag{5.4b}$$

From this it follows that the sum $t_1 + t_2$ is independent of the momentum and thus also independent of the kinetic energy released in the dissociation process. Thus this sum reflects only the instrumental resolution i.e. both the spectrometer factors (temporal resolution and field inhomogeneities) as well as the thermal motion of the parent molecule before dissociation. The same information can also be found in the TOF for the parent ion. In a PE(PI)$^2$CO plot ($t_2$ vs. $t_1$) a distribution with a slope of $-1$ will result for a two-body dissociation. If the charges of the ions are not equal instead a slope of $-q_2/q_1$ is seen [39]. The length of the plot reflects the kinetic energy released whereas the shape of the contour reflects the alignment and thus the geometry of the molecule at the moment of dissociation.

#### PIPICO Spectra

A 2D-projection onto the $t_2 - t_1$ axis for a two-body dissociation, i.e. PhotoIon PhotoIon COincidence (PIPICO), reflects anisotropy and thus the symmetry of the excitation as well as the kinetic energy released in the dissociation process and the geometry of the molecule when dissociating. The geometry at the moment of dissociation is reflected in the shape and the kinetic energy released in the fragmentation is reflected in the width.

By comparing the $t_2 - t_1$ projections with simulations convolved with a peak shape describing the instrumental resolution, the kinetic energy of the dissociation and the symmetry/geometry of the excited state of the molecule can be deduced. This method is used in the analysis of the data in papers I-V. In general there are three different peak shapes seen; rectangular (expected after dissociations with no alignment), "narrow" single peaked (expected after dissociations where most of the momentum is imparted perpendicular to the spectrometer axis) and a double peak structure (expected after dissociations where most of the momentum is imparted parallel with the spectrometer axis).

The overall peak shapes are strong evidence for preserved alignment and rapid dissociation as discussed in Sec. 2.4.2. The values found for $\alpha$ may be underestimated or overestimated.

This because we neglected isotropic contributions (from non resonant component and "long-lived" states which could have time to rotate before dissociation) in the analytic peak shapes. If bond-angle values far from the ground state are found, nuclear motion has occurred and the measured value of $\alpha$ is believed to have contributions from many different geometries.

**PIPICO Peak Shape Simulations**

We derive the functions used to perform the peak shape simulations by assuming preserved molecular alignment as induced by the transition rules of the dipole transitions, see Secs 2.3 and 2.4.2. The derivation is based on paper VII in K. Wiesner's thesis [47].

In polar coordinates the angle-dependent transition probabilities, $P(\theta, \phi)$, for the different dipole moment directions can be expressed as:

$$P_{\mathrm{x}}(\theta,\phi) \propto \sin^2\theta\cos^2\phi \tag{5.5a}$$
$$P_{\mathrm{y}}(\theta,\phi) \propto \sin^2\theta\sin^2\phi \tag{5.5b}$$
$$P_{\mathrm{z}}(\theta,\phi) \propto \cos^2\theta \tag{5.5c}$$

where $\theta$ and $\phi$ are the polar angles between the **e**-vector and the dipole moment.

We can represent an experiment by defining the dipole moment in some fixed coordinate system, preferably the molecular coordinate system, and then rotate the **e**-vector to any possible orientation. For the set-up used here, where the spectrometer axis is parallel to the **e**-vector, the intensity as a function of momentum on the spectrometer axis, $p_0$, can be expressed by the following unnormalized integral:

$$I^*(p_0) = \lim_{\delta\to 0}\frac{1}{\delta}\int_0^{2\pi}\int_{\arccos(p_0+\delta)}^{\arccos p_0} P(\theta,\phi)sin\theta d\theta d\phi. \tag{5.6}$$

where $p_0$ is defined between $-1$ and $1$, and where $-1$ and $1$ imply that all the momentum is distributed along the spectrometer axis and $0$ means that none of the momentum is distributed along the spectrometer axis. Here we integrate over the infinitesimally small momentum interval $\delta p_0$. By inserting the different $P(\theta,\phi)$s from eqns (5.5) we get:

$$I^*_{\mathrm{x}}(p_0) = \pi(1-p_0^2) \tag{5.7a}$$
$$I^*_{\mathrm{y}}(p_0) = \pi(1-p_0^2) \tag{5.7b}$$
$$I^*_{\mathrm{z}}(p_0) = 2\pi p_0^2. \tag{5.7c}$$

The normalized intensities about $p_0$ are instead:

$$I_{\mathrm{x}}(p_0) = \frac{3}{8}(1-p_0^2) \tag{5.8a}$$
$$I_{\mathrm{y}}(p_0) = \frac{3}{8}(1-p_0^2) \tag{5.8b}$$
$$I_{\mathrm{z}}(p_0) = \frac{3}{2}p_0^2. \tag{5.8c}$$

The above derivation is only valid if the main symmetry axis and the bond are parallel, although this is not always true as e.g. for ammonia in paper I and water in paper IV. This is

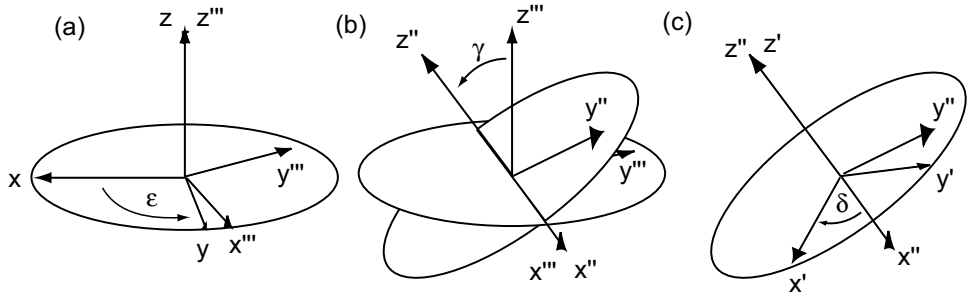


**Figure 5.4**: Illustration of the the Euler rotations used to rotate the molecular frame (unprimed) into the dissociation frame (primed). The figure is based on the figure found in [48].

solved by introducing a new frame, the frame of dissociation (we use a $'$ to denote this frame). This coordinate system is rotated with respect to the molecular frame used in eqns (5.5). This can be described mathematically as:

$$\begin{pmatrix} x' \\ y' \\ z' \end{pmatrix} = R \begin{pmatrix} x \\ y \\ z \end{pmatrix} \tag{5.9}$$

where $R$ is the rotation matrix describing the rotation from the unprimed molecular frame into the primed dissociation frame.

According to Euler's rotation theorem [48], any rotation may be described by using three different angles, illustrated in Fig. 5.4. The first rotation (a) is by an angle $\epsilon$ about the $z$-axis, the second (b) by an angle $\gamma \in [0, \pi]$ about the $x$-axis and the third (c) by an angle $\delta$ about the $z$-axis again. The rotation can be written in terms of a rotation matrices, $A$, $B$ and $C$, expressed as:

$$A = \begin{bmatrix} \cos\epsilon & \sin\epsilon & 0 \\ -\sin\epsilon & \cos\epsilon & 0 \\ 0 & 0 & 1 \end{bmatrix} \tag{5.10}$$

,

$$B = \begin{bmatrix} 1 & 0 & 0 \\ 0 & \cos\gamma & \sin\gamma \\ 0 & -\sin\gamma & \cos\gamma \end{bmatrix} \tag{5.11}$$

and

$$C = \begin{bmatrix} \cos\delta & \sin\delta & 0 \\ -\sin\delta & \cos\delta & 0 \\ 0 & 0 & 1 \end{bmatrix}. \tag{5.12}$$

The total rotation,

$$R = \begin{bmatrix} r_{11} & r_{12} & r_{13} \\ r_{21} & r_{22} & r_{23} \\ r_{31} & r_{32} & r_{33} \end{bmatrix} \tag{5.13}$$

can then be expressed as:

$$R = CBA. \tag{5.14}$$

This produces the different components of $R$:

$$
\begin{aligned}
r_{11} &= \cos\delta\cos\epsilon - \cos\gamma\sin\epsilon\sin\delta && \text{(5.15a)}\\
r_{12} &= \cos\delta\sin\epsilon + \cos\gamma\cos\epsilon\sin\delta && \text{(5.15b)}\\
r_{13} &= \sin\delta\sin\gamma && \text{(5.15c)}\\
r_{21} &= -\sin\delta\cos\epsilon - \cos\gamma\sin\epsilon\cos\delta && \text{(5.15d)}\\
r_{22} &= -\sin\delta\sin\epsilon + \cos\gamma\cos\epsilon\cos\delta && \text{(5.15e)}\\
r_{23} &= \cos\delta\sin\gamma && \text{(5.15f)}\\
r_{31} &= \sin\gamma\sin\epsilon && \text{(5.15g)}\\
r_{32} &= -\sin\gamma\cos\epsilon && \text{(5.15h)}\\
r_{33} &= \cos\gamma. && \text{(5.15i)}
\end{aligned}
$$

By expressing the angle-dependent transition probabilities, eqns (5.5), in the dissociation frame, using eqn (5.9), and solving the different intensity integrals, eqn (5.6), we will after normalization get the following intensities about $p_0$:

$$
\begin{aligned}
I_{\mathrm{x}'}(p_0,\epsilon,\gamma,\delta) &= \frac{3}{8}[(r_{11}^2+r_{12}^2)(1-p_0^2)+4r_{13}^2p_0^2] && \text{(5.16a)}\\
I_{\mathrm{y}'}(p_0,\epsilon,\gamma,\delta) &= \frac{3}{8}[(r_{21}^2+r_{22}^2)(1-p_0^2)+4r_{23}^2p_0^2] && \text{(5.16b)}\\
I_{\mathrm{z}'}(p_0,\epsilon,\gamma,\delta) &= \frac{3}{8}[(r_{31}^2+r_{32}^2)(1-p_0^2)+4r_{33}^2p_0^2]. && \text{(5.16c)}
\end{aligned}
$$

Now we have a general expression for the peak-shapes where the different $r_{\mathrm{ij}}$:s can be found in eqn (5.15). The $r_{\mathrm{ij}}$ coefficients depend on the geometry of the molecule and on the symmetry point group. Three examples follow.

### Peak Shapes for Diatomic Molecules

Diatomic molecules belong to either $\mathrm{D}_{\infty\mathrm{h}}$ (e.g. $\mathrm{N}_2$) or $\mathrm{C}_{\infty\mathrm{v}}$ (e.g. CO). For molecules belonging to these point groups the direction of the bond and the main symmetry axis, $z$, are parallel, thus no rotation is needed and the Euler angles used in eqns (5.16) will all be zero. We thus get the intensity distributions as shown in eqns (5.8). As shown before two types of transitions from a state with $\Sigma$ symmetry are dipole allowed: $\Sigma \rightarrow \Sigma$ and $\Sigma \rightarrow \Pi$. For a $\Sigma \rightarrow \Sigma$ transition the transition probability has its maximum when the **e**-vector is parallel with the bond. Thus the transition probability is expressed as: $P_\Sigma = P_{\mathrm{z}}(\theta,\phi)$. For a $\Sigma \rightarrow \Pi$

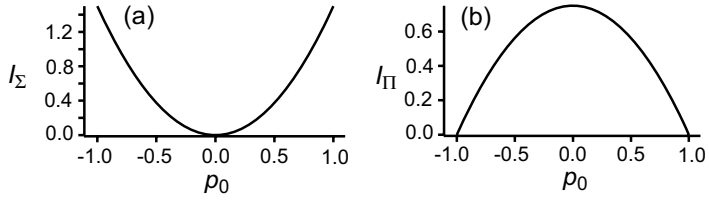


**Figure 5.5**: Analytical profiles for diatomic or linear molecules for (a) $\Sigma - \Sigma$ and (b) $\Sigma - \Pi$ transitions for the **e**-vector parallel to the spectrometer axis.

transition the transition probability has its maximum when the **e**-vector is perpendicular to the bond. The transition probability is thus now expressed as: $P_\Pi = P_\mathrm{x}(\theta,\phi) + P_\mathrm{y}(\theta,\phi)$. The peak shapes is then expressed as:

$$I_\Sigma(p_0) = I_\mathrm{z}(p_0) = \frac{3}{2}p_0^2 \tag{5.17a}$$

$$I_\Pi(p_0) = I_\mathrm{x}(p_0) + I_\mathrm{y}(p_0) = \frac{3}{4}(1-p_0^2), \tag{5.17b}$$

A plot of these analytic peak shapes is found in Fig. 5.5 which are used in papers II and V.

### Peak Shapes for $C_{3v}$ Molecules

In section 2.3.2 we show that there are two allowed transitions from a state with $A_1$ symmetry for molecules belonging to the $C_{3v}$ symmetry point group, namely the $A_1$ to $A_1$ and the $A_1$ to E transitions. The $A_1$ to $A_1$ has its maximum when the polarization vector of the light is parallel to the main symmetry axis, $z$, [see Fig. 5.6 (a)], and the $A_1$ to E transition has its maximum when the polarization vector of the light is in the $x,y$-plane. This leads us once again to the angle-dependent transition probabilities:

$$P_{\mathrm{A}_1} = P_\mathrm{z}(\theta,\phi) \tag{5.18a}$$

$$P_\mathrm{E} = P_\mathrm{x}(\theta,\phi) + P_\mathrm{y}(\theta,\phi). \tag{5.18b}$$

But a difference from the linear case is that the dissociation direction and the dipole moment direction are not parallel; thus we need to perform a rotation. We use the following Euler angles

$$\epsilon = 0 \tag{5.19a}$$

$$\gamma = \alpha \tag{5.19b}$$

$$\delta = 0 \tag{5.19c}$$

to transform from the molecular frame to the dissociation frame. This leads to the following peak shapes:

$$I_{\mathrm{A}_1}(p_0,\epsilon,\gamma,\delta) = I'_\mathrm{z}(p_0,0^\circ,\alpha,0^\circ) = \frac{3}{8}[p_0^2(4-5\sin^2\alpha)+\sin^2\alpha] \tag{5.20a}$$

$$I_\mathrm{E}(p_0,\epsilon,\gamma,\delta) = I'_\mathrm{x}(p_0,0^\circ,\alpha,0^\circ) + I'_\mathrm{y}(p_0,0^\circ,\alpha,0^\circ) = \frac{3}{8}[1+p_0^2(3-5\cos^2\alpha)+\cos^2\alpha]. \tag{5.20b}$$

These are the peak shapes used in paper I to simulate the experimental PIPICO data on ammonia.

### Peak Shapes for $C_{2v}$ Molecules

For molecules belonging to the $C_{2v}$ symmetry point group transitions from a closed shell $A_1$ state is dipole allowed to states with $A_1$, $B_1$ or $B_2$ symmetry with maxima when the light polarization vector is aligned along the molecular $z$, $x$ and $y$ directions, respectively. The

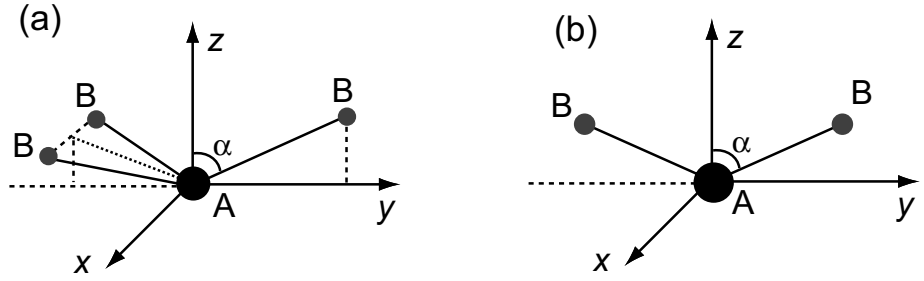


**Figure 5.6**: Molecular coordinate systems for molecules belonging to the $C_{3v}$ (a) and $C_{2v}$ (b) symmetry groups.

molecular coordinate system is defined in Fig. 5.6 (b). This leads us to the angle-dependent transition probabilities:

$$P_{\mathrm{A}_1} = P_{\mathrm{z}}(\theta,\phi) \quad (5.21a)$$
$$P_{\mathrm{B}_1} = P_{\mathrm{x}}(\theta,\phi) \quad (5.21b)$$
$$P_{\mathrm{B}_2} = P_{\mathrm{y}}(\theta,\phi). \quad (5.21c)$$

But the dissociation direction and the transition dipole moment direction are not parallel; thus as in the former case we need to perform rotations using the following angles:

$$\epsilon = 0 \quad (5.22a)$$
$$\gamma = \alpha \quad (5.22b)$$
$$\delta = 0. \quad (5.22c)$$

In this case $\alpha$ is half the bond angle. This gives us to the following intensity distributions:

$$I_{A_1}(p_0,\epsilon,\gamma,\delta) = I'_{\mathrm{z}}(p_0,0^\circ,\alpha,0^\circ) = \frac{3}{8}[p_0^2(4-5\sin^2\alpha)+\sin^2\alpha] \quad (5.23a)$$
$$I_{B_2}(p_0,\epsilon,\gamma,\delta) = I'_{\mathrm{y}}(p_0,0^\circ,\alpha,0^\circ) = \frac{3}{8}[p_0^2(4-5\cos^2\alpha)+\cos^2\alpha] \quad (5.23b)$$
$$I_{B_1}(p_0,\epsilon,\gamma,\delta) = I'_{\mathrm{x}}(p_0,0^\circ,\alpha,0^\circ) = \frac{3}{8}[1-p_0^2]. \quad (5.23c)$$

These are the peak shapes used in papers II, III and IV for $O_3$, $SO_2$and $H_2O$, respectively.

### 5.2.2 Three-body Processes

A good way to get an upper limit on the time frame for dissociation in multi-step processes is to study the shape of the contour plots for these reactions. Multi-step dissociation where the time interval between the dissociation steps is long enough for the molecule to rotate is expected to have the shape of a parallelogram constructed of superimposed ellipses [49]. On the other hand, if the time interval is fast enough so that little or no rotation occurs only one of these superimposed ellipses will contribute to the shape. Thus if contour plots show an elliptical shape, as in all plots presented in this thesis, the upper limit for the dissociation time is determined by the rotational period.

Lets consider the multi-step dissociations in more detail. We disregard rotation between the dissociation steps and assume that the time scale is large enough so the fragment ejected from the first step does not influence step two. The sequential dissociation process can be expressed as:

$$\text{Step 1:} \quad \text{ABC} \rightarrow \text{AB} + \text{C} + U_1 \tag{5.24a}$$
$$\text{Step 2:} \quad \text{AB} \rightarrow \text{A} + \text{B} + U_2 \tag{5.24b}$$

where $U_1$ and $U_2$ are the kinetic energy released in each step which can be expressed:

$$U_1 = \frac{1}{2} m_{\text{AB}} v_{\text{AB}}^2 + \frac{1}{2} m_{\text{C}} v_{\text{C}}^2 \tag{5.25a}$$
$$U_2 = \frac{1}{2} m_{\text{A}} v_{\text{A}}^2 + \frac{1}{2} m_{\text{B}} v_{\text{B}}^2. \tag{5.25b}$$

Here $m_{\text{X}}$ and $v_{\text{X}}$ are the mass and velocity of fragment X, respectively. The time of flight for the different fragments can be written:

$$t_{\text{A}} = t_{\text{A}}^0 + a m_{\text{A}} v_{\text{A}} \cos\eta_{\text{A}} \tag{5.26a}$$
$$t_{\text{B}} = t_{\text{B}}^0 + a m_{\text{B}} v_{\text{B}} \cos\eta_{\text{B}} \tag{5.26b}$$
$$t_{\text{C}} = t_{\text{C}}^0 + a m_{\text{C}} v_{\text{C}} \cos\eta_{\text{C}}, \tag{5.26c}$$

where $\cos\eta_{\text{A}}$ is the angle between the initial momentum and the spectrometer axis, $a m_{\text{X}} v_{\text{X}} \cos\eta_{\text{X}}$ is half the "turn around" time and $t_{\text{X}}^0$ is the average time of flight for fragment X, respectively. Conservation of momentum lead to the following:

$$m_{\text{C}} v_{\text{C}} + m_{\text{AB}} v_{\text{AB}} = 0 \tag{5.27a}$$
$$m_{\text{C}} v_{\text{C}} - m_{\text{AB}} v_{\text{AB}} = \mathbf{p} \tag{5.27b}$$
$$m_{\text{B}} v_{\text{B}} + m_{\text{A}} v_{\text{A}} = 0 \tag{5.27c}$$
$$m_{\text{B}} v_{\text{B}} - m_{\text{A}} v_{\text{A}} = \mathbf{q}. \tag{5.27d}$$

Here **p** and **q** are the total momentum in the first and second dissociation steps.

Now we have the foundation for examining coincident detection of two of the fragments A, B or C and seeing how **p** and **q** will affect the $t_1$ vs. $t_2$ contour plots. Depending on the relative direction of **p** and **q** according to their projections along the spectrometer axis we get different results. Let's start with the case indicated in top of Fig. 5.7. For this system the flight times can be rewritten as:

$$t_{\text{A}} = t_{\text{A}}^0 + \frac{a}{2}\left(-q - \frac{m_{\text{A}}}{m_{\text{AB}}} p\right) \tag{5.28a}$$
$$t_{\text{B}} = t_{\text{B}}^0 + \frac{a}{2}\left(q - \frac{m_{\text{B}}}{m_{\text{AB}}} p\right) \tag{5.28b}$$
$$t_{\text{C}} = t_{\text{C}}^0 + \frac{a}{2} p, \tag{5.28c}$$

where $q$ and $p$ is the amount of momentum projected onto the spectrometer axis and positive initial direction is moving away from the spectrometer. Thus the positive direction is to the left in the figure.

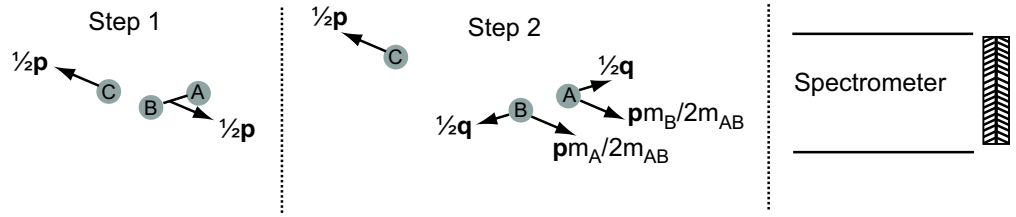


Detecting C and A where C is heavier than A

(a) $t_2=t_C$ $t_1=t_A$

slope = $-m_{AB}/m_A$

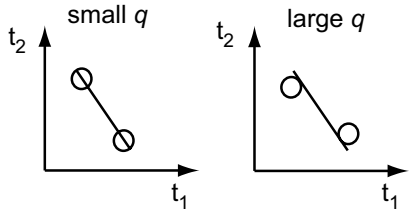


Detecting C and A where A is heavier than C

(b) $t_2=t_A$ $t_1=t_C$

slope = $-m_A/m_{AB}$

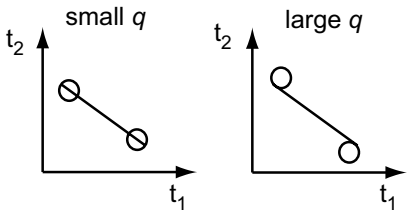


Detecting C and B where C is heavier than B

(c) $t_2=t_C$ $t_1=t_B$

slope = $-m_{AB}/m_B$

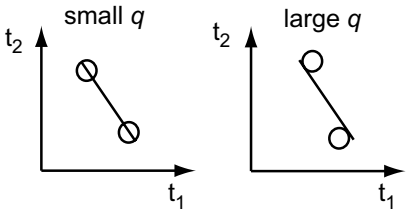


Detecting C and B where B is heavier than C

(d) $t_2=t_B$ $t_1=t_C$

slope = $-m_B/m_{AB}$

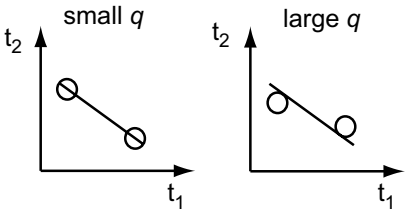


Detecting A and B where A is heavier than B

(e) $t_2=t_A$ $t_1=t_B$

slope = -1

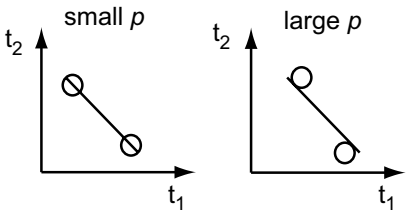


Detecting A and B where B is heavier than A

(f) $t_2=t_B$ $t_1=t_A$

slope = -1

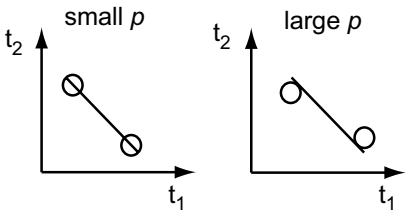


**Figure 5.7**: Sketches of the dependence on the $t_2$ vs. $t_1$ plots originating from the momentum released in the dissociation step where one of the fragments is not detected in a sequential three-body dissociation. See the text for more detail.

**Detecting A and C** Lets first consider the case when fragment C is the heavier one, thus $t_2 = t_{\mathrm{C}}$ and $t_1 = t_{\mathrm{A}}$. By combining eqns (5.28c) and (5.28a) we then get:

$$t_1 = t_{\mathrm{A}}^0 + \frac{a}{2}\left(-q - \frac{m_{\mathrm{A}}}{m_{\mathrm{AB}}}p\right) \tag{5.29a}$$

$$t_2 = \left(t_{\mathrm{C}}^0 + \frac{m_{\mathrm{AB}}}{m_{\mathrm{A}}}t_{\mathrm{A}}^0\right) - \frac{m_{\mathrm{AB}}}{m_{\mathrm{A}}}t_1 - \frac{am_{\mathrm{AB}}}{2m_{\mathrm{A}}}q. \tag{5.29b}$$

Thus a slope of $-\frac{m_{\mathrm{AB}}}{m_{\mathrm{A}}}$ is expected in the $t_2$ vs. $t_1$ plot. But if the contribution from $q$ is large the last term will also contribute and displace the area where the maximum intensity is located. In this case when fragment C has "longer" flight times (upper left intensity maximum in the plot) the contribution from $q$ will result in slightly shorter flight time for fragment C ($t_2$) and as well slightly shorter flight times for fragment A ($t_1$), see eqns (5.29). This is depicted in Fig. 5.7 (a). For a description of the lower right intensity maximum the opposite orientation is considered. Now the terms in eqns (5.28), and thus also the terms in eqns (5.29), containing $p$ or $q$ will have opposite sign. Thus the displacement in this case will be as indicated in the figure.

If fragment A is the heavier one, $t_2 = t_{\mathrm{A}}$ and $t_1 = t_{\mathrm{C}}$, we get:

$$t_1 = t_{\mathrm{C}}^0 + \frac{a}{2}p \tag{5.30a}$$

$$t_2 = \left(t_{\mathrm{A}}^0 + \frac{m_{\mathrm{A}}}{m_{\mathrm{AB}}}t_{\mathrm{C}}^0\right) - \frac{m_{\mathrm{A}}}{m_{\mathrm{AB}}}t_1 - \frac{a}{2}q. \tag{5.30b}$$

Thus in this case we get a slope of $-\frac{m_{\mathrm{A}}}{m_{\mathrm{AB}}}$ instead and $q$ will only influence $t_2$. In this case we look on the lower right part of the plot and the upper left part can be described by treating the opposite orientation. This result is sketched in Fig. 5.7 (b).

**Detecting B and C** This resembles the case above when A and C were detected. The difference is in the direction of $q$, so the plots will look very much different. For the case of C heavier than B ($t_2 = t_{\mathrm{C}}$ and $t_1 = t_{\mathrm{B}}$) we get:

$$t_1 = t_{\mathrm{B}}^0 + \frac{a}{2}\left(q - \frac{m_{\mathrm{B}}}{m_{\mathrm{AB}}}p\right) \tag{5.31a}$$

$$t_2 = \left(t_{\mathrm{C}}^0 + \frac{m_{\mathrm{AB}}}{m_{\mathrm{B}}}t_{\mathrm{B}}^0\right) - \frac{m_{\mathrm{AB}}}{m_{\mathrm{B}}}t_1 + \frac{am_{\mathrm{AB}}}{2m_{\mathrm{B}}}q. \tag{5.31b}$$

So a slope of $-\frac{m_{\mathrm{AB}}}{m_{\mathrm{B}}}$ is expected in this case. But again if $q$ is large enough it will be seen in the plot. In this case, where we treat the upper left intensity maximum, the contribution from $q$ will result in a slightly longer flight-time for fragment C ($t_2$) and as well as a slightly longer flight-time for fragment B ($t_1$), see eqns (5.31). A sketch of this is seen in Fig. 5.7 (c).

Going to the case of B heavier than C we will get:

$$t_1 = t_{\mathrm{C}}^0 + \frac{a}{2}p \tag{5.32a}$$

$$t_2 = \left(t_{\mathrm{B}}^0 + \frac{m_{\mathrm{B}}}{m_{\mathrm{AB}}}t_{\mathrm{C}}^0\right) - \frac{m_{\mathrm{B}}}{m_{\mathrm{AB}}}t_1 + \frac{a}{2}q. \tag{5.32b}$$

Thus a slope of $-\frac{m_{\mathrm{B}}}{m_{\mathrm{AB}}}$ is expected instead. The contribution from $q$ on the lower right intensity maximum, we treat in this case, is positive as seen in Fig. 5.7 (d).

**Detecting A and B** The last case to consider is when detecting the two fragments from the last step in the dissociation, A and B. We start to treat the case when A is heavier than B, thus $t_2 = t_{\mathrm{A}}$ and $t_1 = t_{\mathrm{B}}$, we get:

$$t_1 = t_{\mathrm{B}}^0 + \frac{a}{2}\left(q - \frac{m_{\mathrm{B}}}{m_{\mathrm{AB}}}p\right) \tag{5.33a}$$

$$t_2 = t_{\mathrm{A}}^0 + t_{\mathrm{B}}^0 - t_1 - \frac{a}{2}p. \tag{5.33b}$$

Thus a slope of $-1$ is expected in the $t_2$ vs. $t_1$ contour plot but again the maximum can be displaced by the influence from the momentum in the dissociation step releasing an undetected fragment, $p$ in this case. Taking $p$ into account we get the displacement as indicated in Fig. 5.7 (e). This treatment is valid for the lower right part of the $t_2$ vs. $t_1$ plot.

In the case of B heavier than A ($t_2 = t_{\mathrm{B}}$ and $t_1 = t_{\mathrm{A}}$) we get:

$$t_1 = t_{\mathrm{A}}^0 + \frac{a}{2}\left(-q - \frac{m_{\mathrm{A}}}{m_{\mathrm{AB}}}p\right) \tag{5.34a}$$

$$t_2 = t_{\mathrm{B}}^0 + t_{\mathrm{A}}^0 - t_1 - \frac{a}{2}p. \tag{5.34b}$$

Thus the same behavior as above but this time the heavy fragment moves away from the detector and we treat the upper left part of the plot. Also the influence from $p$ on $t_1$ will be slightly different depending on the masses. This is sketched in Fig. 5.7 (f).

In case of the orientation as indicated in top of Fig. 5.8 the sign for the $q$ term in eqns (5.28a) and (5.28b) is opposite. Thus the displacement plots for the case of detecting A and C or B and C will be interchanged. Also the plots detecting A and B will differ depending on which fragment is heavier. Thus for this orientation we will get the plots as illustrated in Fig. 5.8.

Yet another mechanism is possible for a three-body dissociation, fast concerted dissociation. In this mechanism the two bonds holding ABC together are ruptured simultaneously. Thus the time scale is not large enough so that conservation of momentum can be applied to the steps in (5.24), we get instead:

$$\mathrm{ABC} \rightarrow \mathrm{A} + \mathrm{B} + \mathrm{C}. \tag{5.35}$$

In general the expected slope is hard to predict, but if the undetected fragment has a small amount of momenta, a slope of -1 is expected. Also an overall ovoid shape is expected [50].

**$H_2O$ as an example** In Fig. 5.9 the $H^+$+$O^+$ data measured at the two core excited states, O $1s^{-1}4a_1^1$ and O $1s^{-1}2b_2^1$, is shown (paper IV). In the top of the figure the preferential alignment of the molecules after resonant excitation at the energies used is shown. The two plots show very different behaviors attributed to the difference in preferred alignment and possible the dissociation mechanisms. The sequential dissociation of water can be described in the following way:

$$\text{Step 1:} \quad \mathrm{HOH} \rightarrow \mathrm{HO} + \mathrm{H} \tag{5.36a}$$

$$\text{Step 2:} \quad \mathrm{HO} \rightarrow \mathrm{H} + \mathrm{O} \tag{5.36b}$$

where the total momentum in the first step is **p** and in the second step is **q**. If we detect an $H^+$, $O^+$ pair the hydrogen fragment can, in principle, come from either the first or the

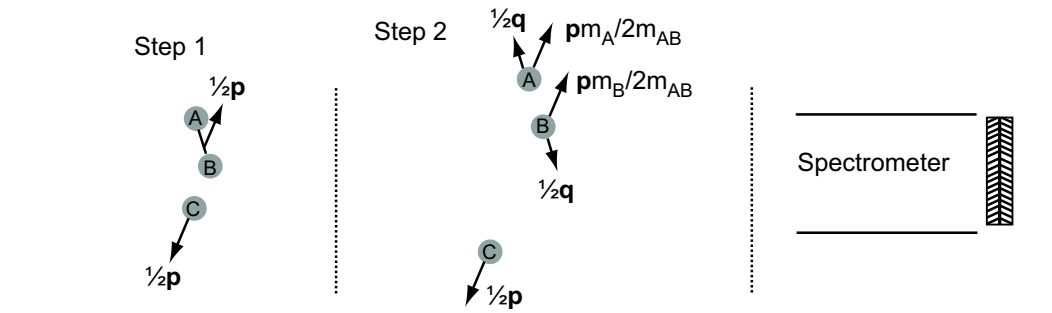


Detecting C and A where C is heavier than A

(a) $t_2=t_C$ $t_1=t_A$

slope = $-m_{AB}/m_A$

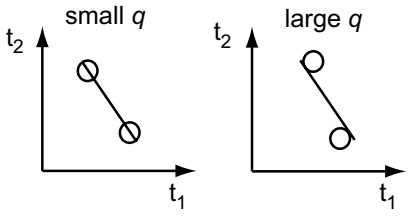


Detecting C and A where A is heavier than C

(b) $t_2=t_A$ $t_1=t_C$

slope = $-m_A/m_{AB}$

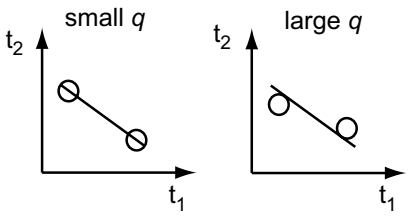


Detecting C and B where C is heavier than B

(c) $t_2=t_C$ $t_1=t_B$

slope = $-m_{AB}/m_B$

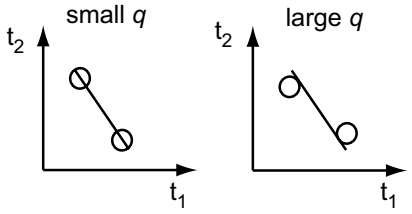


Detecting C and B where B is heavier than C

(d) $t_2=t_B$ $t_1=t_C$

slope = $-m_B/m_{AB}$

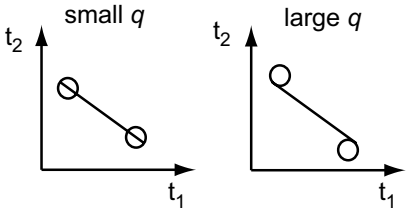


Detecting A and B where A is heavier than B

(e) $t_2=t_A$ $t_1=t_B$

slope = -1

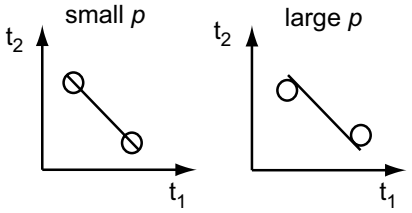


Detecting A and B where B is heavier than A

(f) $t_2=t_B$ $t_1=t_A$

slope = -1

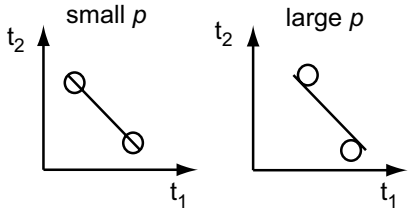


**Figure 5.8**: Sketches of the dependence on the $t_2$ vs. $t_1$ plots originating from the momentum released in the dissociation step where one of the fragments is not detected in a sequential three-body dissociation. See the text for more detail.

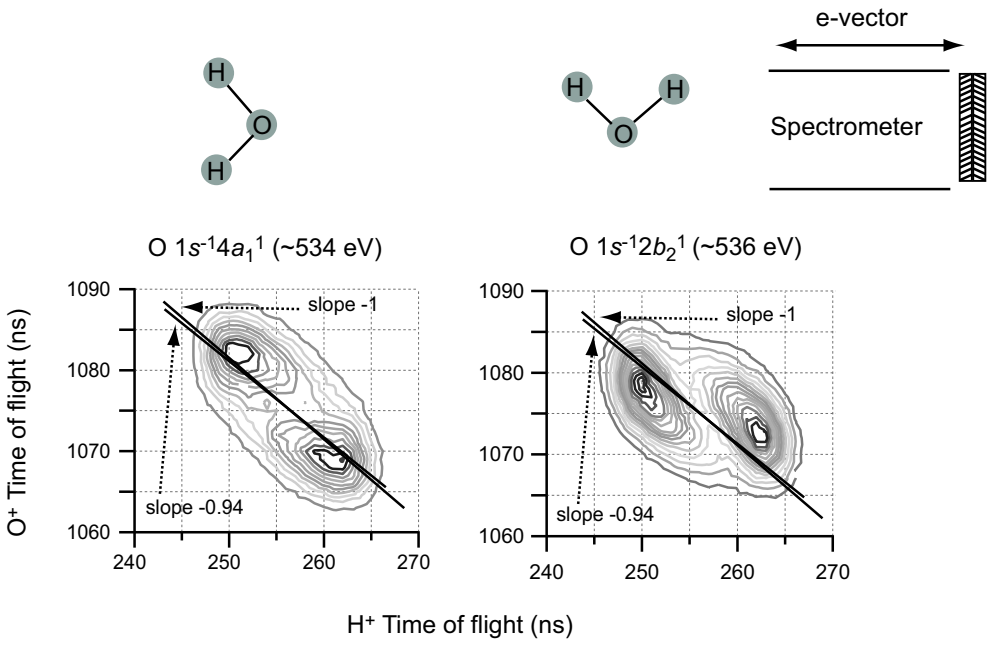


**Figure 5.9**: PE(PI)$^2$CO plots measured at the photon energy of the O $1s^{-1}4a_1^1$ and O $1s^{-1}2b_2^1$ states. In the upper part the expected alignment for each measurement is shown. The lines in the plots are drawn as a guide to the expected slope without any momentum given to the undetected H fragment and are taken from Fig. 5.7 (d) and (f) and 5.8 (d) and (f). See the text for discussion.

second dissociation step. It is very hard to distinguish these two cases in the experimental data. This because the slope expected for processes without any momentum given to the undetected fragment is similar, $-\frac{m_{\mathrm{O}}}{m_{\mathrm{HO}}} = -0.94$ and -1. At the same time the contribution from eventual momentum to the undetected fragment will give the same kind of contribution in the two sequential cases, see Figs. 5.7 (d) and (f) and 5.8 (d) and (f) for the two possible orientations. However, we can conclude that the PE(PI)$^2$CO plot maps the expected preferential alignment and that the undetected fragment caries away more momentum in the O $1s^{-1}2b_2^1$ measurement.

## 5.3 Mass Spectroscopy on Clusters

By performing mass spectroscopy measurements on clusters information on the size of the clusters, the kind of fragments formed, the amount of these fragments and the kinetic energy released can be gained.This is crucial information in studies on rare-gas clusters where different ionization mechanisms lead to different dissociation pathways. A limitation on mass spectroscopic measurements on clusters is the large amount of uncondensed atoms in the cluster beam. Thus the atomic signal depends mainly on these uncondensed atoms.

The shape of a peak in a mass-spectrum depends among other things on the kinetic energy distributions of the fragments projected along the spectrometer axis. This is reflected in the broadening of the peaks. A kinetic energy scale on each peak can be obtained from:

$$U_{\mathrm{k}} = \frac{(qE_{\mathrm{s}}\Delta t)^2}{2m} \tag{5.37}$$

where $U_{\mathrm{k}}$ is the kinetic energy of the fragment along the spectrometer axis and $\Delta t$ is the time difference from ions with zero kinetic energy.

Ionization of rare-gas clusters normally results in "metastable" states with lifetimes ranging from some ps to some $\mu$s. Thus the decay occurs both in the accelerations and/or drift tube regions giving different contributions to the time of flight peak shapes. To study this effect in our spectra we have developed a model, in which we numerically calculate the time of flight distributions in the spectrometer. The trajectories are calculated classically solving the motion equations of charged particles using the 4th order Runge-Kutta algorithm [51]. We used an initial isotropic distribution of "mother" fragments, with initial kinetic energy, $\mathrm{KE_m}$, and lifetime, $\tau_{\mathrm{m}}$. Thus the number of mother ions, $N$, decrease with time as:

$$N_{\mathrm{m}}(t) = N_0 e^{-t/\tau_{\mathrm{m}}}, \tag{5.38}$$

and the number of daughter fragments increase with time:

$$N_{\mathrm{d}}(t) = -\frac{dN_{\mathrm{m}}(t)}{dt} = N_0/\tau_{\mathrm{m}} e^{-t/\tau_{\mathrm{m}}}. \tag{5.39}$$

The daughter ion is assumed to be emitted isotropically with a variable kinetic energy depending on the kinetic energy released in the dissociation, $\mathrm{KE_{rel}}$, and the masses of the mother and the daughter, $m_{\mathrm{m}}$ and $m_{\mathrm{d}}$, respectively. From conservation of momentum we thus get:

$$\mathrm{KE_d} = \mathrm{KE_{rel}}(m_{\mathrm{m}} - m_{\mathrm{d}})/m_{\mathrm{m}}. \tag{5.40}$$

The peak shapes are then simulated using a Monte-Carlo integration convoluted with our instrumental broadening. To understand the results of the simulation two cases must be considered, dissociation of the mother-ion before entering the drift tube or after. Inthe case of mother ion dissociation in the acceleration regions the daughter ion arrive with a short time of flight and the peak is asymmetric. The asymmetry is due to the exponential decay as described in eqn (5.40). This peak is independent of the extraction condition as well as the kinetic energies $\mathrm{KE_m}$ and $\mathrm{KE_{rel}}$, but depends on the ratio $m_{\mathrm{d}}/m_{\mathrm{m}}$. If instead the mother ion dissociates in the drift tube the daughter ion arrives almost at the same time of flight as the mother ion. The peak shape is symmetric and the time spread is related to the kinetic energy imparted to the daughter ion as well as to the original speed of the mother ion and the length of the drift tube.

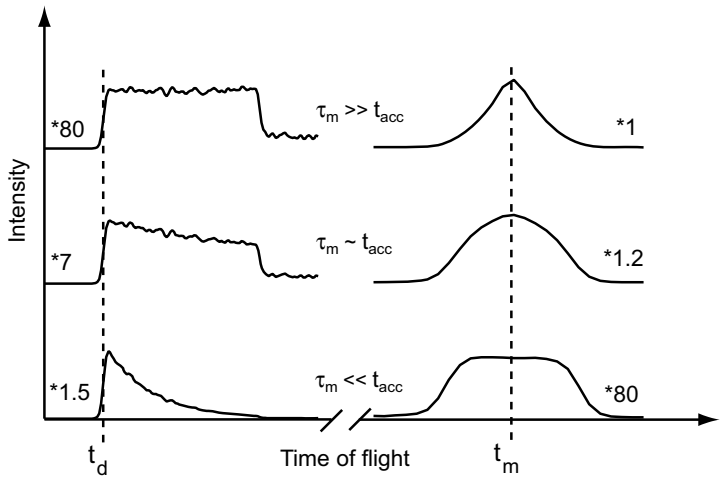


**Figure 5.10**: Time of flight distributions for daughter and mother ions for different lifetimes of the mother ion, $\tau_{\mathrm{m}}$. The time of flight of the daughter and mother fragments are indicated by $t_{\mathrm{d}}$ and $t_{\mathrm{m}}$, respectively. The scaling factor is given in order to compare the absolut peak height.

We simulated the peaks shown in Fig. 5.10. Argon dimers are used as mother ions and monomers as daughters. The time of flight of the daughter and mother fragments are indicated by $t_{\mathrm{d}}$ and $t$m, respectively. Three typical cases are shown: $\tau_{\mathrm{m}} >> t_{\mathrm{acc}}$, $\tau_{\mathrm{m}} \sim t_{\mathrm{acc}}$ and $\tau_{\mathrm{m}} << t_{\mathrm{acc}}$, where $t_{\mathrm{acc}}$ is the travel time for the mother ion from the source point to the entrance of the drift tube ($\sim$ 300 ns in our case). We used mother ion decay times in the different cases as follows: $\tau_{\mathrm{m}} = 3600$ ns, $\tau_{\mathrm{m}} = 300$ ns and $\tau_{\mathrm{m}} = 50$ ns going from the upper case to the lower. For long $\tau_{\mathrm{m}}$s as in the upper case of Fig. 5.10, almost no signal will appear at $t_{\mathrm{d}}$, the influence from the decay in the drift tube on the mother ion peak will show up as an "Eiffel-tower" shape. For the other extreme with very short $\tau_{\mathrm{m}}$s a "metastable tail" mapping the decay time will be seen in the daughter peak shape whereas the mother ion peak shape will be almost unaffected. Also in the case of $\tau_{\mathrm{m}}$ close to $t_{\mathrm{acc}}$ a "metastable tail" appears in the daughter ion peak shape, although less pronounced this time. The peak shape of the mother ion will in this case be "rounder" than in the case of $\tau_{\mathrm{m}} >> t_{\mathrm{acc}}$.

Chapter 6

# Summary of Papers

## 6.1 Ion-coincidence Measurements of Small Molecules

### 6.1.1 Paper I: Molecular Alignment of Ammonia Studied by Electron-ion-ion Coincidence Spectroscopy

Ion coincidence measurements were carried out near the N $1s$ threshold in ammonia. The absorption spectrum shows five distinct spectral features. We performed measurements on each of these features and in addition we also scanned the photon energy through the first two, assigned to the N $1s \rightarrow 4a_1^*$ and N $1s \rightarrow 2e^*$ transitions. The aim of the study was to explore alignment effects upon resonant core excitation and to study the time frame of dissociation. Information about molecular geometry and symmetry for the excited states was found. The geometry and symmetry were deduced by comparing the experimental data with simulations for the two body dissociations ($H^+ + NH_2^+$). The time frame of dissociation can be understood by studies of preserved alignment for the three and four body dissociations.

The study gave new information on the symmetry character and geometric rearrangement of the different excited states. Evidence for rapid dissociation (faster than the rotation) was also found in the preserved alignment in the three- and four-body dissociation processes. Moreover the detuning of the N $1s \rightarrow 4a_1$ transition shows that the kinetic energy released upon fragmentation together with the geometry of the molecule changes. This is clear indication of a repulsive potential surface and significant valence character for this transition.

### 6.1.2 Paper II: Core-Excited Electronic States and Fragmentation of Ozone – Analytic Tools and Experiment

Ion coincidence measurements after resonant excitation near the $O_T 1s$ and $O_C 1s$ thresholds in ozone are presented. Core excitation was made from both central and terminal oxygen and differences in the fragmentation between these are discussed. In order to map out the excitation energies a high-resolution high-purity ion yield spectrum is presented. The symmetry of the excitations was investigated by comparing the peak shape of the two-body $O^+ + O_2^+$ dissociations with analytic peaks shape functions, by eye. Also the effect of ultra fast dissociation of the $O_T 1s^{-1} 7a_1^1$ state was studied.

Different fragmentation patterns for the central and terminal core excitations are revealed,

from this, together with the position in energy, strong indication of that the dominant transition at 540 eV is $O_C 1s \rightarrow 7a_1^*$. From the fragmentation patterns and the ion-ion coincidence measurements we were also able to confirm the effect of ultra-fast dissociation and the localized $\sigma$-like character of the $O_T 1s \rightarrow 7a_1$ excitation.

### 6.1.3 Paper III: Absence of Symmetry Breaking Observed for O $1s$ Core-excited Sulfur Dioxide

O $1s$ core-excited sulfur dioxide is studied with the help of both ion coincidence measurements and configuration interaction (CI) calculations. The alignment effect and thus the symmetry at some different excited states is studied. Via the fragmentation measurement also the kinetic energy released in the $O^+$+$SO^+$ dissociation processes as well as the dissociation mechanisms at the different excited states are found.

From the alignment studies we find three different classes of alignment, one along each of the three molecular coordinate axes. This is strong evidence on that a non-localized picture with preserved symmetry is best used to describe the transitions. The difference in slopes of the $O^+$+$S^+$ channel in the PE(PI)$^2$CO plots, gave information on the dissociation mechanisms at the various excited states, and a development towards faster neutral evaporation was seen. Also signs of nuclear rearrangements before dissociation were found for the states with $B_2$ symmetry, indicating a dissociation slower than one vibrational period.

### 6.1.4 Paper IV: Resonant Electron-ion Coincidence Measurements of Water Near the Oxygen K-edge

Again core excitation of the states just below the oxygen K-edge was studied, this time for water. In the PE(PI)$^2$CO plot of the three-body process $H^+$+$O^+$+$H^?$ large momentum of the undetected hydrogen fragment was found. To describe this a model of the sequential three-body dissociation was introduced. Clear sign of alignment of the core-excited states was again seen. Studying the geometry changes we found a closing bend angle for the O $1s^{-1}2b_2^1$ state with respect to the ground state but no major changes for the O $1s^{-1}4a_1^1$ state. The latter is a clear indication of very rapid dissociation (fs-scale).

### 6.1.5 Paper V: Description and Performance of an Electron-ion coincidence TOF Spectrometer Used at the Brazilian Synchrotron Facility LNLS

The paper is a characterization of the electron-ion coincidence time of flight spectrometer used at the Brazilian synchrotron facility LNLS. The spectrometer is of the same two-field type as the one described in this thesis with a major difference; in order to improve the detection efficiencies and allow the use of relatively small diameter detectors, lenses used to focus the ions and electrons are used. My main contribution to this paper is the simulations of the PIPICO data of $N_2$ measured at the so called N $1s \rightarrow \sigma^*$ shape resonance at 420 eV. The simulations revealed that the transition is an overlap of 65% $\sigma^*$ character and 35% $\pi^*$ character and also that the polarization degree at the beam line is $\sim$85%.

## 6.2 Photo Fragmentation of Argon Clusters

### 6.2.1 Paper VI: Photon Energy Dependence of Fragmentation of Small Argon Clusters

Photo-fragmentation of small argon clusters (<N>$= 5$) is reported. The studies are performed by ion time of flight measurements with different photon energies around the Ar $2p$ threshold. It is seen that the cluster fragments produced below the Ar $2p_{3/2} \rightarrow 4s$ resonance have low kinetic energy, as expected when single ionization is dominant. At the $2p_{3/2} \rightarrow 4s$ resonance the $Ar_2^+$ production is enhanced while above the Ar $2p$ threshold almost complete atomization is observed. In the two latter cases the kinetic energy imparted to the fragments is large indicating that multiply charged clusters are formed before dissociation. Together, these experimental observations cannot be explained in a simple "Coulomb explosion" model invoking charge separation, which would simply lead to complete atomization with no dependence on the photon energy. The observed processes can be rather well understood in a molecular approach assuming that the adiabatic double ionization potential (DIP) is at much lower energy that the vertical DIP and the internal energy left in the cluster depends on the excited ionic electronic state.

### 6.2.2 Paper VII: Size Dependence Fragmentation of Argon Clusters

Fragmentation of argon clusters of an average size of 10 to 1000 atoms using a photon energy of 116 eV are studied with our multi-coincidence spectrometer. In order to understand the peak shapes of the metastable clusters, a model describing the influence from decay half-lives ranging from picoseconds (ps) to microseconds ($\mu$s) is described.

Clear evidence for different dissociation dynamics is seen. For small clusters (<N>$\sim 10$) fast neutral evaporation (ps) before slow ($\mu$s) degradation of the cluster ion is observed. For large (<N>$\geq 100$) clusters the behavior is very different. The large unstable multiply-charged clusters fragment into small singly ionized species in a time scale in the order of 100 nanoseconds (ns). Again a slow ($\mu$s) degradation of the ionic clusters is observed, as in the case of small clusters, is seen.

# Bibliography


[1] J. Eland, F. Wort, and R. Royds, J. Electron Spectrosc. Relat. Phenom. **41**, 297 (1986).

[2] L. Frasinski, M. Stankiewicz, K. Randall, P. Hatherly, and K. Codling, J. Phys. B **19**, L819 (1986).

[3] M. Simon, T. Lebrun, P. Morin, M. Lavollée, and J. L. Maréchal, Nucl. Instrum. Methods Phys. Res., Sect. B **62**, 167 (1991).

[4] D. Hanson, C. Ma, K. Lee, D. Lapiano-Smith, and D. Kim, J. Chem. Phys. **93**, 9200 (1990).

[5] N. Saito and I. H. Suzuki, Phys. Rev. Lett. **61**, 2740 (1988).

[6] N. Saito, F. Heiser, O. Hemmers, K. Wieliczek, J. Viefhaus, and U. Becker, Phys. Rev. A **54**, 2004 (1996).

[7] N. Kosugi, J. Electron Spectrosc. Relat. Phenom. **79**, 351 (1996).

[8] K. Ueda, K. Ohmori, M. Okunishi, H. Chiba, Y. Shimizu, Y. Sato, T. Hayaishi, E. Shigemasa, and A. Yagishita, Phys. Rev. A **52**, R1815 (1995).

[9] H. Yoshida, K. Nobusada, K. Okada, S. Tanimoto, N. Saito, A. D. Fanis, and K. Ueda, Phys. Rev. Lett. **88**, 083001 (2002).

[10] Y. Muramatsu, K. Ueda, N. Saito, H. Chiba, M. Lavolle, A. Czasch, T. Weber, O. Jagutzki, H. Schmidt-Bcking, R. Moshammer, U. Becker, K. Kubozuka, and I. Koyano, Phys. Rev. Lett **88**, 133002 (2002).

[11] N. Saito, Y. Muramatsu, H. Chiba, K. Ueda, K. Kubozuka, I. Koyano, K. Okada, O. Jagutzki, A. Czasch, T. Weber, M. Hattass, H. Schmidt-Bocking, R. Moshammer, M. Lavollee, and U. Becker, J. Electron Spectrosc. Relat. Phenom. **141**, 183 (2004).

[12] N. Saito, A. D. Fanis, I. Koyano, and K. Ueda, Physica Scripta **T110**, 90 (2004).

[13] M. Machida, M. Lavolle, J. Randrianjafisoa, G. Laurent, M. Nagoshi, K. Okada, I. Koyano, and N. Saito, J. Chem. Phys. **120**, 3635 (2004).

[14] A. De Fanis, N. Saito, M. Machida, K. Okada, H. Chiba, A. Cassimi, R. Drner, I. Koyano, and K. Ueda, Phys. Rev. A **69**, 022506 (2004).

[15] J. Stöhr, *NEXAFS Spectroscopy* (Springer-Verlag, Heidelberg, Germany, 1992).

[16] T. Koopmans, Physica **1**, 104 (1934).

[17] P. W. Atkins, in *Physical Chemistry*, 6th ed. (Oxford University press, Great Clarendon Street, Oxford OX2 6DP, England, 2001), Chap. 15, pp. 427–448.

[18] J. M. Hollas, in *Modern Spectroscopy*, 4th ed. (John Wiley & Sons, Ltd, The Atrium, Southern Gate, Chichester, West Sussex PO19 8SQ, England, 2004), Chap. 7.3.2, pp. 275–277.

[19] J. Somers, A. W. Robinson, T. Lindner, D. Ricken, , and A. M. Bradshaw, Phys.Rev. B **40**, 2053 (1989).

[20] G. Herzberg, *Molecular Spectra and Moleular Structure III. Electronic spectra and electronic structure of polyatomic molecules* (Krieger Publ. comp., Malabar, Florida, 1991).

[21] H. Oji and N. Kosugi, *Ab initio CI Calculation of Transition Dipole Moment for* $\mathrm{O}1s \rightarrow \sigma^*(7a_1)$ *Core-excitation of Ozone* (unpublished).

[22] P. Morin and I. Nenner, Phys Rev. Lett. **56**, 1913 (1986).

[23] O. Björneholm, J. Chem. Phys. **115**, 4139 (2001).

[24] R. Wetmore, R. L. Roy, and R. Boyd, J. Phys. Chem. **88**, 6318 (1984).

[25] A. Slattery, T. Field, M. Ahmad, R. Hall, J. Lambourne, F. Penent, P. Lablanquie, and J. Eland, J. Chem. Phys. **122**, 84317 (2005).

[26] R. N. Zare, Mol. Photochem **4**, 1 (1972).

[27] J. Bozek, N. Saito, and I. Suzuki, Phys. Rev. A **51**, 4563 (1995).

[28] T. Gejo, Y. Takata, T. Hatsui, M. Nagasono, H. Oji, N. Kosugi, and E. Shigemasa, Chem. Phys. **289**, 15 (2003).

[29] H. Haberland, Surf. Scien. **156**, 305 (1985).

[30] E. Rühl, Int. J. Mass Spectrom. **229**, 117 (2003).

[31] R. Casero, J. Saenz, and J. Soler, Phys. Rev. A **37**, 1401 (1988).

[32] E. Rühl, C. Heinzel, H. Baumgärtel, M. Lavollée, and P. Morin, Z. Phys. D **31**, 245 (1994).

[33] E. Rühl, C. Schmale, H. W. Jochims, E. Biller, M. Simon, and H. Baumgärtel, J. Chem. Phys. **95**, 6544 (1991).

[34] A. De Fanis, M. Oura, N. Saito, M. Machida, M. Nagoshi, A. Knapp, J. Nickles, A. Czash, R. Dörner, Y. Tamenori, H. Chiba, M. Takahashi, J. H. D. Eland, and K. Ueda, J. Phys. B. **37**, L235 (2004).

[35] M. Tchaplyguine, R. Feifel, R. R. T. Marinho, M. Gisselbrecht, S. L. Sorensen, A. N. de Brito, N.Mårtensson, S.Svensson, and O. Björneholm, Chem.Phys. **289**, 3 (2003).

[36] R. Karnbach, M. Joppien, J. Stapelfeldt, J.Wörmer, and T. . Möller, Rev. Sci. Instrum. **64**, 2838 (1993).

[37] W. C. Wiley and I. H. McLaren, Rev. Scien. Instr. **26**, 1150 (1955).

[38] J. Jauhiainen, S. Aksela, and E. Nommiste, Physica Scripta **51**, 549 (1995).

[39] J. Eland, Molecular Physics **61**, 725 (1987).

[40] D. A. Dahl, *Simion 3D version 7.0 User's manual*, Idaho National Engineering and Environmental Laboratory, 2000.

[41] www.burle.com.

[42] www.ortec-online.com.

[43] www.phillipsscientific.com.

[44] www.fastcomtec.com.

[45] www.fastcomtec.com/fwww/aptof.htm.

[46] www.wavemetrics.com.

[47] K. Wiesner, Ph. d. thesis, Uppsala University, University Library, Box 510, 75120 Uppsala, 2003, paper VII.

[48] http://mathworld.wolfram.com/eulerangles.html.

[49] M. Simon, T. Lebrun, R. Martins, G. G. B. de Souza, I. Nenner, M. Lavollee, and P. Morin, J. Phys. Chem. **97**, 5228 (1993).

[50] J. H. D. Eland, Laser Chem. **11**, 259 (1991).

[51] W. H. Press, S. A. Teukolsky, W. T. Vetterling, and B. P. Flannery, in *Numerical recipes in C* (Cambridge University Press, The Edinburgh Building, Cambridge CB2 2RU, UK, 1999), Chap. 16, pp. 707–747.